SOFT ROBOTICS
Volume 00, Number 00, 2020
© Mary Ann Liebert, Inc.
DOI: 10.1089/soro.2019.0082

SoRo
Soft Robotics

Octopus Arm-Inspired Tapered Soft Actuators with Suckers for Improved Grasping

Zhexin Xie,[1,2,*] August G. Domel,[3,*] Ning An,[3] Connor Green,[3] Zheyuan Gong,[1] Tianmiao Wang,[1] Elias M. Knubben,[4] James C. Weaver,[5] Katia Bertoldi,[3] and Li Wen[1]

Downloaded by Harvard University FRANCIS A COUNTWAY from www.liebertpub.com at 02/28/20. For personal use only.

Abstract

Octopuses can employ their tapered arms to catch prey of all shapes and sizes due to their dexterity, flexibility, and gripping power. Intrigued by variability in arm taper angle between different octopus species, we explored the utility of designing soft actuators exhibiting a distinctive conical geometry, compared with more traditional cylindrical forms. We find that these octopus-inspired conical-shaped actuators exhibit a wide range of bending curvatures that can be tuned by simply altering their taper angle and they also demonstrate greater flexibility compared with their cylindrical counterparts. The taper angle and bending curvature are inversely related, whereas taper angle and applied bending force are directly related. To further expand the functionality of our soft actuators, we incorporated vacuum-actuated suckers into the actuators for the production of a fully integrated octopus arm-inspired gripper. Notably, our results reveal that because of their enhanced flexibility, these tapered actuators with suckers have better gripping power than their cylindrical-shaped counterparts and require significantly larger forces to be detached from both flat and curved surfaces. Finally, we show that by choosing appropriate taper angles, our tapered actuators with suckers can grip, move, and place a remarkably wide range of objects with flat, nonplanar, smooth, or rough surfaces, as well as retrieve objects through narrow openings. The results from this study not only provide new design insights into the creation of next-generation soft actuators for gripping a wide range of morphologically diverse objects but also contribute to our understanding of the functional significance of arm taper angle variability across octopus species.

Keywords: octopus arm, tapered soft actuator, bending and suction

Objective

Biological systems have inspired the design of a wide range of materials and devices capable of addressing modern engineering challenges.[1–8] Octopuses represent one such example. They can effectively catch prey of different shapes and sizes, perform remarkably complex tasks, and retrieve objects from constrained environments by combining two important capabilities: (1) the ability to control many degrees of freedom and (2) the integration of linear arrays of suckers (Fig. 1A–C).[9–14] Because of their flexibility, agility, and adaptability for efficiently grasping a wide range of structurally diverse objects, octopus arms have served as model systems for the development of robust soft robotic prototypes. These range from single powerful actuators[15–19] to more complex multi-actuator systems.[20–24] These soft robots offer many advantages over their more traditional rigid counterparts in that they are significantly easier and cheaper to manufacture, are safer to operate around human subjects, and can achieve complex outputs with simple inputs.[25–35] Despite the fact that octopus arms exhibit a characteristic conical geometry and that the taper angle is highly variable between different species, many soft actuators (including octopus-inspired forms) exhibit a constant cross-

[1]School of Mechanical Engineering and Automation, Beihang University, Beijing, China.
[2]Shenyuan Honors College, Beihang University, Beijing, China.
[3]John A. Paulson School of Engineering and Applied Sciences, Harvard University, Cambridge, Massachusetts.
[4]Leitung Corporate Bionic Department, Festo SE & Co. KG, Germany.
[5]Wyss Institute of Biologically Inspired Engineering, Harvard University, Cambridge, Massachusetts.
*These authors contributed equally to this work.

Downloaded by Harvard University FRANCIS A COUNTWAY from www.liebertpub.com at 02/28/20. For personal use only.

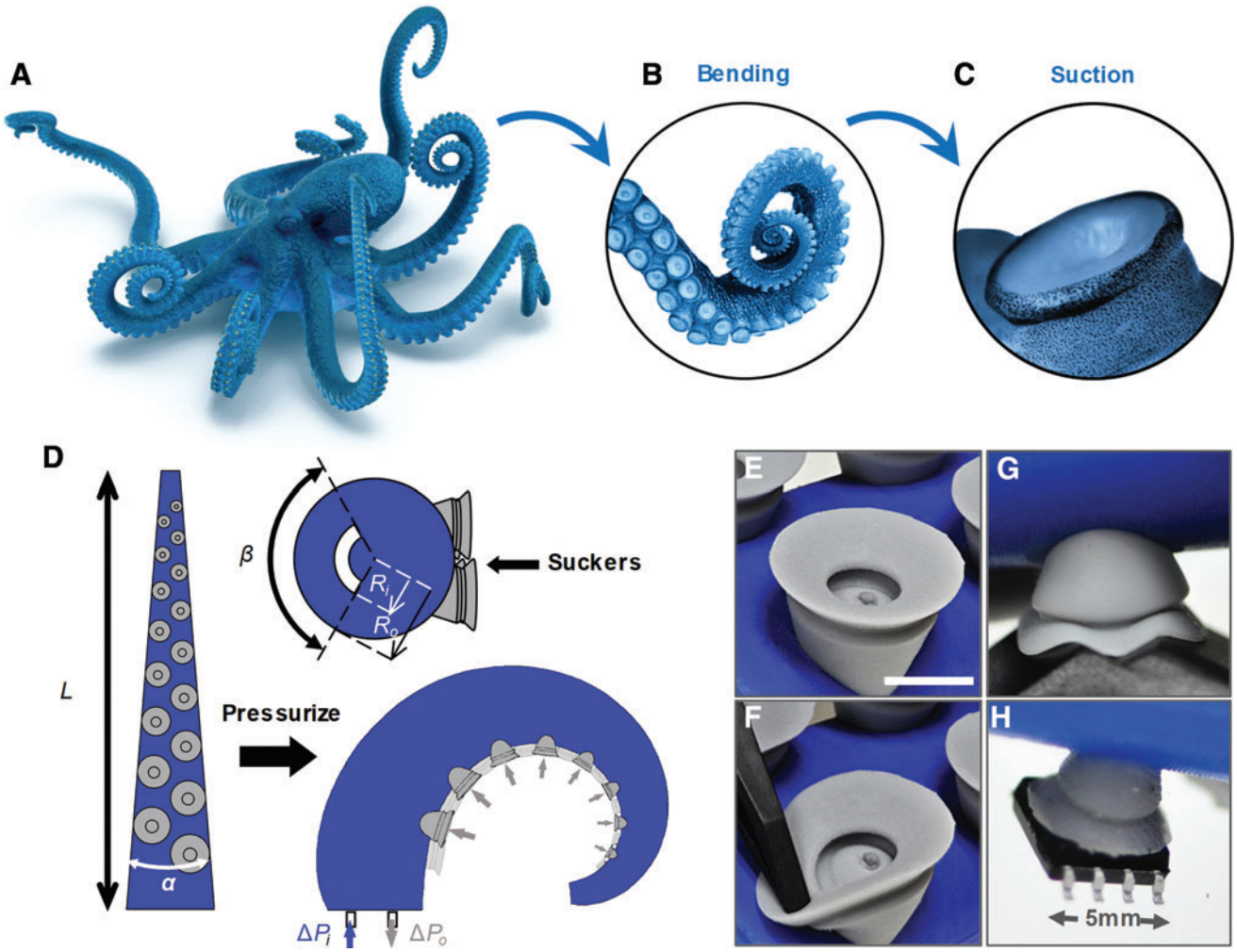

FIG. 1. Octopus arm-inspired tapered soft actuators with suckers for improved grasping. **(A–C)** Octopus arms are tapered and incorporate both bending and suction functionalities. Here, we use them as inspiration for the design of soft robotic actuators with improved grasping. **(D)** Schematics of our tapered soft actuators with suckers. **(E–H)** Our suckers are flexible, conformable, and can attach to small objects. Scale bar in panel **(E)**, 1 cm. Color images are available online.

sectional diameter along their length.[24,27–31] Little is known regarding the functional significance of this diversity, however, as previous studies on octopus-inspired tapered soft actuators have focused on the control of the arm motion.[15–22] While the subject of modeling passive bending of tapered cantilever beams has received some attention,[36] little research has been done on soft robotics which can grasp or manipulate objects.

Inspired by investigations into the morphological diversity of octopus arms, we explore the potential trade-offs between dexterity and gripping power in tapered soft actuators. In contrast to previous studies on octopus-inspired robots, which focused primarily on either arm motion[15–22] or sucker action alone,[37–40] in this study we focus on the (1) tapered arm and (2) the synergistic function of bending and suction. We first numerically study the bending kinematics and applied forces of tapered soft actuators, and then use these findings to guide the design and fabrication of an octopus arm-inspired soft robot with integrated suckers for improved gripping (Fig. 1D–H).

Materials and Methods

Details on the measurements performed to estimate the taper angle of living specimens can be found in Section S1 of the Supplementary Data. The design geometry of the tapered actuator and its suckers investigated in this study is detailed in Section S2 of the Supplementary Data. The fabrication details of the tapered soft actuators used in the validation of the finite element (FE) simulations and the characterization of the material mechanical response can be found in Section S3 of the Supplementary Data. The bending curvature and bending force experiments on tapered soft actuators without suckers can be found in Section S4 of the Supplementary Data. The FE simulations for bending curvature and applied bending force were conducted with Abaqus (SIMULIA, Providence, RI), and details can be found in Section S5 of the Supplementary Data. Using the insights from the results of the FE simulations, the tapered actuators with suckers were ultimately fabricated with a multistep molding and casting process. The tapered soft actuators were made of Mold Star

30 (Smooth-On, Inc., PA), and the suckers were made of Dragon Skin FX-Pro (Smooth-On, Inc.). Details for this fabrication can be found in Section S6 of the Supplementary Data. The experiments of sucker attachment forces are detailed in Section S7 of the Supplementary Data. And finally, demonstrations of the complete tapered actuators with suckers can be found in Section S8 of the Supplementary Data.

Results

Octopus arms

In this study, we focus on two important features of octopus arms: the taper angle and the combination of arm bending and suction. Since a systematic investigation on the taper angle range of octopus arms was not available to guide our study, we performed detailed measurements from online photographs of living specimens[41] acquired from 10 different octopus species (Section S1 of the Supplementary Data and Supplementary Fig. S1). While there are extremes in arm taper angle, such as the exceptionally broad arms found in *Abdopus gorgonos*, we found that for most species, arm taper angles ranged from a minimum of ca. 3° for the very slender arms of *Octopus macropus* to a maximum of ca. 13.5° for the comparatively broader arms found in *Eledone cirrhosa* (Fig. 2, see Supplementary Table S1 for detailed data). Guided by these measurements, we considered taper angles ranging from $\alpha = 3°$ to $\alpha = 13.5°$ and investigated their effects on both actuator bending curvature and applied bending force in the present study.

In most octopus species, two rows of suckers are distributed in a staggered arrangement along the ventral surface of each arm, with diameters ranging from a few millimeters to a few centimeters.[11,42] They comprise an exposed disk-like *infundibulum* and a central cavity *acetabulum* and allow for strong attachment not only to large flat surfaces but also to irregular surfaces, and even objects smaller than a single sucker.[43,44] In this study, we mimicked this general structure and distribution when designing our soft robotic suckers for integration into our tapered soft actuators. Although much simpler than their natural counterpart, these biomimetic suckers provide a similar function. Upon application of vacuum, they enable the actuator to attach to arbitrary objects.

Effect of taper angle on bending curvature and applied bending force

We first investigated, numerically, via FE simulations, the properties of tapered pneumatic soft actuators (without suckers), focusing on the effect of the taper angle on both bending curvature and applied bending force. Specifically, we considered tapered soft actuators, each of the same length ($L = 200$ mm) and tip diameter ($D_{tip} = 8.4$ mm), but with taper angles ranging from $\alpha = 3°$ to $\alpha = 13.5°$ (see Section S2 of the Supplementary Data for more design details). To induce bending via inflation, a single hollow internal chamber was placed along the length of the actuator at a fixed normalized distance from the outer radius of the actuator. The internal chamber was tapered in the same manner as that of the actuator, and the cross-sectional shape of the chamber was annular, swept 120° (see Section S2 of the Supplementary

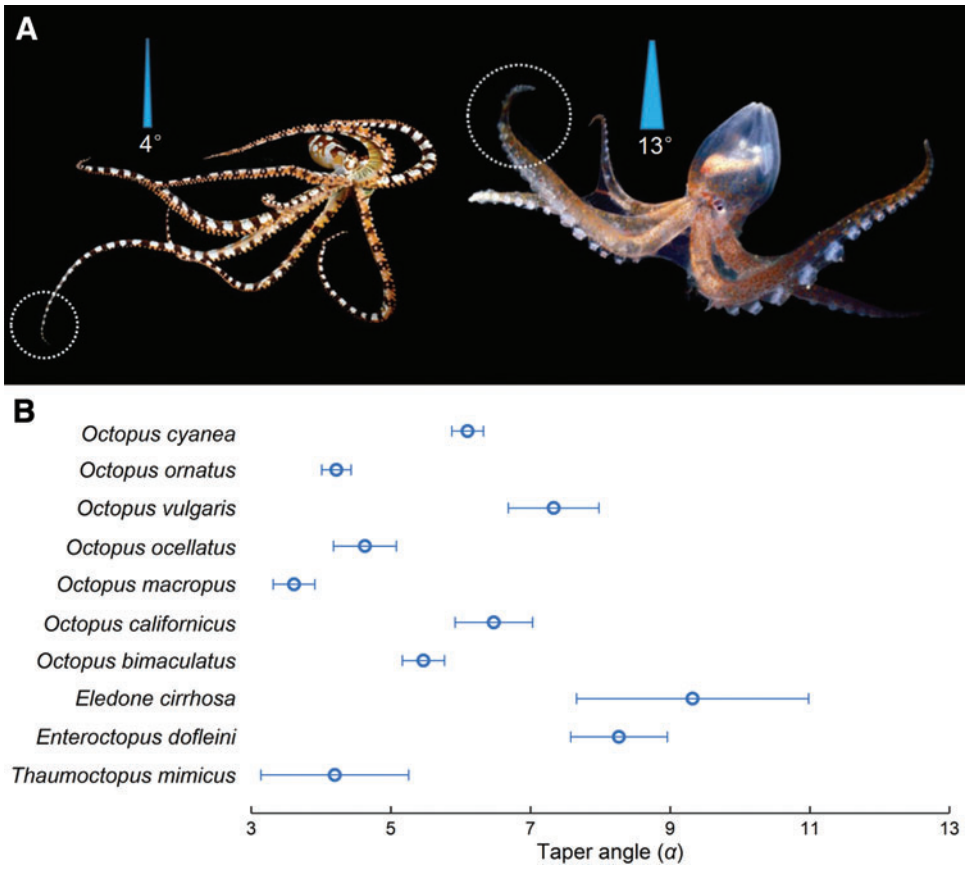

FIG. 2. Arm taper angle diversity among various octopus species. **(A)** Photographs of two representative octopus species that exhibit low (*left*, *Wunderpus photogenicus*) and high (*right*, *Vitrelladonella richardi*) arm taper angles. **(B)** Taper angle measurements (all data are provided in Supplementary Table S1) from 10 different octopus species (multiple individuals of each species were considered). Octopus photos courtesy of Roy Caldwell and Solvin Zankl. Color images are available online.

Downloaded by Harvard University FRANCIS A COUNTWAY from www.liebertpub.com at 02/28/20. For personal use only.

Downloaded by Harvard University FRANCIS A COUNTWAY from www.liebertpub.com at 02/28/20. For personal use only.

Data and Supplementary Fig. S3 for more details and schematics on the internal chamber).

For FE studies, all models were constructed using 8-node linear brick elements (Abaqus element type C3D8H), and the material behavior was captured using an incompressible Gent model,[45] with initial shear modulus $\mu = 195$ kPa and stiffening parameter $J_m = 12$ (see Section S3 of the Supplementary Data for more details). Static nonlinear simulations were performed using Abaqus/Standard and, to induce bending, each actuator's inner chamber was pressurized from $P = 0$ kPa to $P = 200$ kPa with the bottom end of the actuator being held in a fixed position. To evaluate the effect of the taper angle on the bending curvature, no additional constraint was added, and at each incremental 2 kPa increase in pressure, the maximum, minimum, and average curvature along the bending profile of the actuator was measured (see Section S4 of the Supplementary Data for more details). To study the effect of taper angle on applied bending force, the actuators were placed at a horizontal distance $d = 30$ mm away from a rigid body surface (representing a hypothetical load cell) and frictional surface to surface contact (with a coefficient of friction of 0.5) was employed between the actuator and the hypothetical load cell. When an input pressure was applied to each of these actuators (with the actuator base fixed), they would bend toward this rigid surface and the applied force was monitored.

We first validated our numerical simulations by comparing the numerical results with those obtained experimentally for actuators fabricated from Mold Star 30 (Smooth-On, Inc.) silicone rubber (Sections S4 of the Supplementary Data and Supplementary Figs. S12 and S14). Since we found an excellent agreement between the two data sets in terms of both bending curvature and bending force over a wide range of pressures, we then proceeded to use FE simulations for a much more extensive exploration of the actuator design space. We started by numerically investigating the effect of the taper angle on the bending curvature. The results shown in Figure 3A demonstrate that the bending curvature of the tapered actuators depend highly on both the taper angle α and the pneumatic pressure P. Specifically, the bending curvature increases as pressure P increases, but decreases as the taper angle α increases. For example, the average bending curvature (κ) decreased by over twofold (from $\kappa = 0.0282\ \text{mm}^{-1}$ to $\kappa = 0.0134\ \text{mm}^{-1}$) by increasing the taper angle from $\alpha = 3°$ to $\alpha = 13.5°$ at $P = 200$ kPa, and changed from $\kappa = 0.0009\ \text{mm}^{-1}$ to $\kappa = 0.0134\ \text{mm}^{-1}$ by increasing the pneumatic pressure from $P = 100$ kPa to $P = 200$ kPa for $\alpha = 13.5°$ (see Section S5 of the Supplementary Data and Supplementary Fig. S13 for more detailed simulation results of bending curvature). It should also be noted that for a given pressure and taper angle, the maximum, minimum, and average curvatures varied along the length of the actuator, thus permitting the grasping of different sized objects at a single actuating pressure.

After characterizing bending curvature as a function of taper angle, we next investigated the exerted bending force as a function of pressure. Interestingly, the numerical results reported in Figure 3B show that the taper angle produced opposite responses in terms of bending force and bending curvature (Fig. 3B and see Section S4 of the Supplementary Data and Supplementary Fig. S11 for results of other measured distances other than $d = 30$ mm). For example, the bending force increased from 0.33 to 5.35 N when the taper angle was increased from $\alpha = 3°$ to $\alpha = 13.5°$ at $P = 200$ kPa (Fig. 3B), whereas the bending curvature decreased from $\kappa = 0.0282\ \text{mm}^{-1}$ to $\kappa = 0.0134\ \text{mm}^{-1}$ when the taper angle was increased from $\alpha = 3°$ to $\alpha = 13.5°$ at $P = 200$ kPa (Fig. 3A). Therefore, when taking both the bending force and bending curvature results into account, we discovered an inherent trade-off between the two. Overall, models with lower taper angles output a lower force but could bend with much larger curvature (with the opposite being true for larger taper angles).

The complete octopus arm-inspired prototype

Guided by these numerical results, we then investigated how the taper angle affected the gripping power of a soft actuator with integrated suckers. To this end, 17 silicone rubber suction cups (made from Dragon Skin FX-Pro; Smooth-On, Inc.) were integrated into the design using a multistep molding process and arranged in a staggered

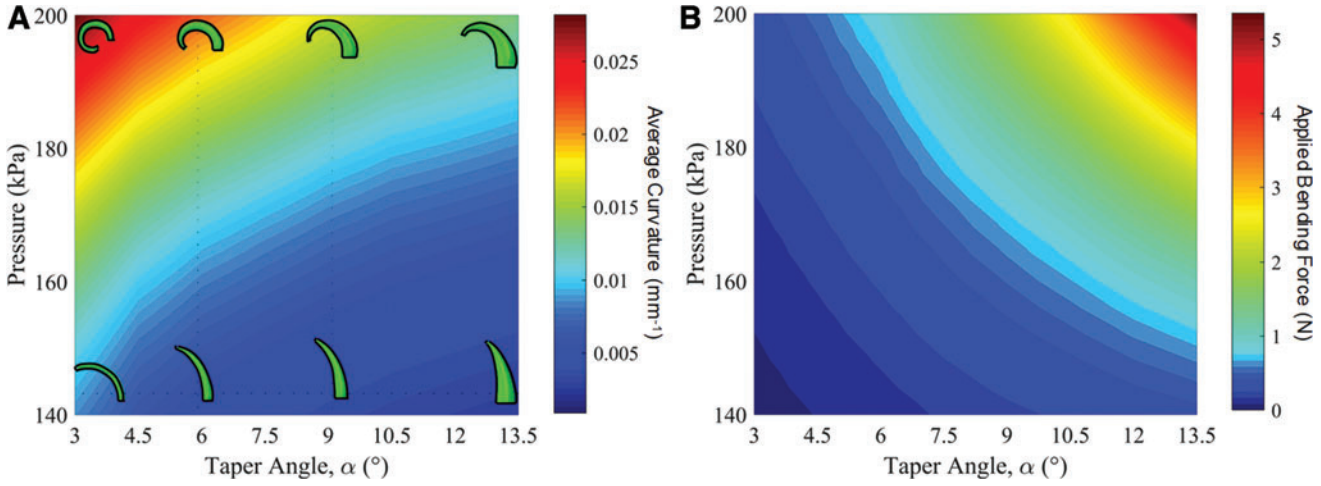

FIG. 3. Modeling the effects of arm taper angle on bending curvature and applied bending force. **(A)** Numerical results illustrating the average bending curvature (κ) as a function of taper angle (α) and input pressure (P). Bending profile snapshots obtained from the simulations at $P = 150$ kPa and $P = 200$ kPa are overlaid on the heat map. **(B)** Numerical results illustrating the applied bending force (FN) as a function of taper angle (α) and input pressure (P). Color images are available online.

Downloaded by Harvard University FRANCIS A COUNTWAY from www.liebertpub.com at 02/28/20. For personal use only.

pattern along the length of the actuator (Fig. 1 and Section S6 of the Supplementary Data and Supplementary Fig. S15). The flexible suckers were designed and fabricated by mimicking the geometries of the *infundibulum* and *acetabulum* of *Octopus vulgaris* (Fig. 1C).[46] Moreover, for the sake of simplicity, they were all connected to a single-channel vacuum generator which was used to lower the pressure inside each of the suckers. Upon evacuation, the suckers could conform and attach to a wide range of different-sized objects (Fig. 1H), and even those with irregular surfaces (Fig. 1G). We constructed both a cylindrical and an $\alpha = 9°$ tapered actuator with suckers and characterized the attachment behavior of their suckers to substrates exhibiting a variety of different geometries and surface roughnesses (see Section S7 of the Supplementary Data for details). Note that in the tapered gripper, the size of the suction cups decreased from the base of the actuator to the tip, as is seen in its biological counterpart (Supplementary Fig. S4). In contrast, the cylindrical gripper used suction cups which were all identical and dimensionalized to provide the same total suction area as in the tapered gripper (Supplementary Fig. S5).

Attachment abilities characterization

We began by characterizing the attachment of the cylindrical and tapered grippers to planar substrates (Fig. 4A) since planar objects are often difficult to grasp using bending actuators alone. In these tests, we first lowered the pressure inside the suckers from 0 to −80 kPa to fully attach the suction cups to the surface and then pulled the grippers in the direction perpendicular to the surface while recording the force via a substrate-integrated load cell. Remarkably, we found that the enhanced flexibility of the tapered gripper results in significantly higher gripping power. Specifically, the results shown in Figure 4A–C show two key features. First, the pull-off force (i.e., the maximum force recorded during the test) recorded for a tapered gripper (6.59 ± 0.32 N) is significantly higher than that measured for the cylindrical one (5.61 ± 0.24 N) (Fig. 4C). Second, the mechanism by which the two grippers eventually detach from the surface is qualitatively different. While suckers of the tapered gripper detached from the surface in a sequential manner (Fig. 4A, B, Supplementary Movies S1 and S2), resulting in a post-yield stairstep-like

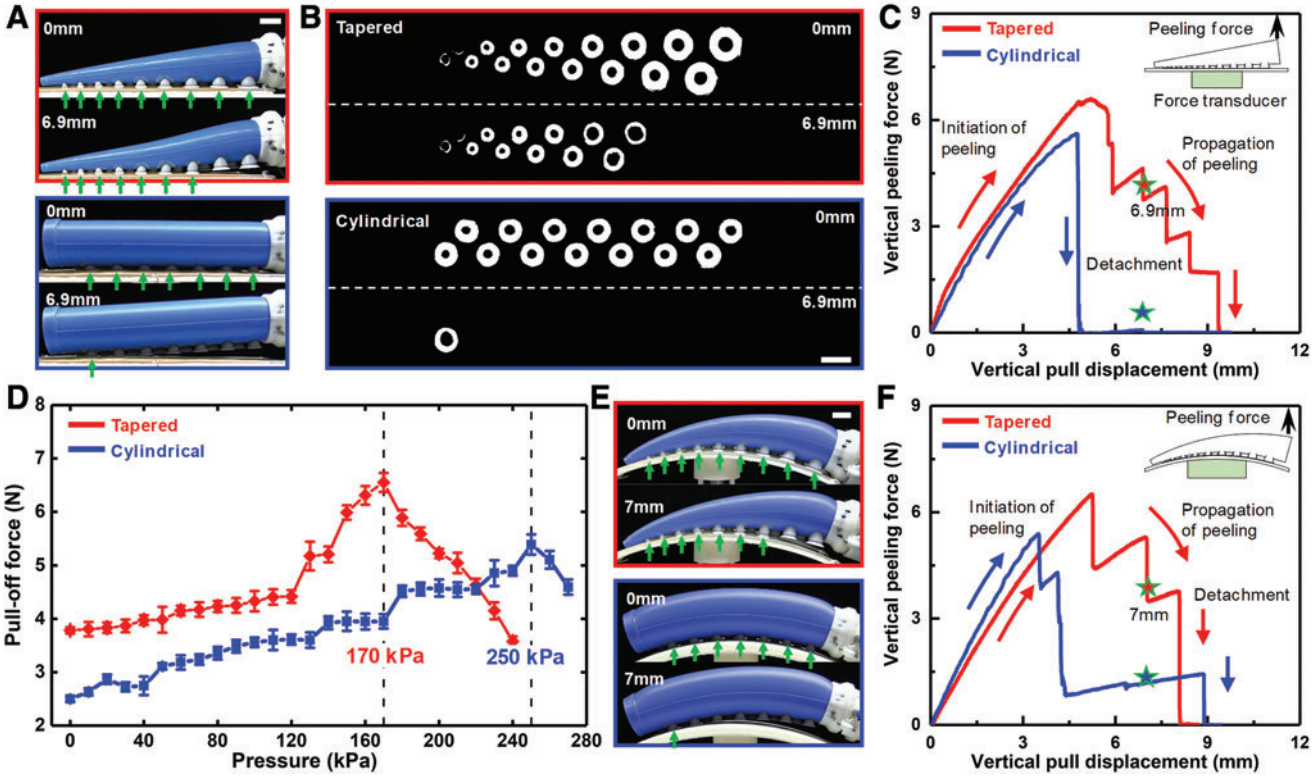

FIG. 4. Sucker attachment force and contact measurements. **(A)** Side view photographs showing the sequential peeling of the tapered ($\alpha = 9°$) actuator with suckers, and the simultaneous peeling of the cylindrical actuator with suckers from a smooth planar surface (scale bar, 20 mm). The *blue arrows* indicate the suckers that are attached to the surface during peeling. **(B)** Frustrated total internal reflection[47] images highlighting the attachment of the suckers (see also Supplementary Movie S2) (scale bar, 20 mm). **(C)** Load–displacement curves recorded during the peeling test for both the tapered and cylindrical actuators with suckers. The peeling force is measured along the vertical direction. **(D)** Scanning a wide range of input pressures permits the identification of the optimal input pressures for maximizing pull-off forces of both actuators with suckers from nonplanar substrates. The *vertical dashed line* indicates the ''optimal'' pneumatic pressure values for maximizing the pull-off forces for the curvature of this specific surface ($260\ \text{mm}^{-1}$). **(E)** Side view photographs showing the sequential peeling of an $\alpha = 9°$ actuator with suckers, and the almost simultaneous peeling of the cylindrical actuator with sucker from a smooth curved surface (scale bar, 20 mm). **(F)** Load–displacement curves recorded during the peeling test for both the tapered and cylindrical actuators with suckers. The peeling force is measured along the vertical direction. Color images are available online.

Downloaded by Harvard University FRANCIS A COUNTWAY from www.liebertpub.com at 02/28/20. For personal use only.

failure mode (Fig. 4C), the reduced flexibility of the cylindrical one prevented such behavior and led to simultaneous detachment of all suckers (Fig. 4A, B, Supplementary Movies S1 and S2), inducing a sharp drop in force (Fig. 4C).

We next characterized the attachment abilities of the actuators with suckers to curved surfaces and focused on a surface with curvature 1/260 mm^{-1}. The results shown in Figure 4D demonstrate that the attachment to the surface for both the tapered and cylindrical grippers was highly dependent on the pressure, with the maximum pull-off forces recorded at $P = 170$ and 250 kPa, respectively. When such pressure is applied, the actuators best approximated the curved surface, and the suckers were fully engaged and provided maximum gripping power. Notably, in this case we found that the enhanced flexibility of the tapered actuator resulted in a larger maximum pulling force (6.55 ± 0.18 N). It is also important to note that both soft grippers could achieve almost identical pull-off force on the flat and curved surfaces (Fig. 4C, F). This behavior was enabled by the intrinsic compliance of the actuators that allowed them to conform to arbitrarily shaped objects so that all suckers could engage with the surface. To completely eliminate the impact of the sucker size and distribution on the attachment performance, we also tested a cylindrical gripper with suckers of identical size and distribution to those of our tapered design. As shown in Supplementary Figure S19, we found that in this case also, all the cylindrical gripper suckers peeled off nearly simultaneously, resulting in a sharper and more sudden failure compared with the tapered design. These results further support our conclusion that the tapered actuator with suckers has better gripping power than its cylindrical counterpart.

Due to their compliant nature, the suckers were also able to successfully attach to surfaces exhibiting a wide range of surface roughnesses (Fig. 5A–C), but exhibited pronounced performance trade-offs which varied as a function of sucker modulus. For example, the $\alpha = 9°$ gripper with stiff suckers (Young's modulus 660 kPa) generated a considerable pull-off force of up to 26.14 ± 0.54 N (error values ± standard error of the mean) on relatively smooth surfaces (R_a <20 μm), which represented a nearly fourfold increase over that of the $\alpha = 9°$ gripper with flexible suckers (Young's modulus 250 kPa) (Fig. 5D). Despite this performance advantage on smooth surfaces, and due to their reduced flexibility, the stiffer suckers exhibited a reduced ability to conform to more topographically complex surfaces (e.g., $R_a = 200$ μm in Fig. 5), highlighting the need to consider sucker modulus when exploring the suitable application space of the gripper.

Grasping applications

After characterizing the sucker's capabilities and required peeling forces, we explored the real-world applications of our tapered grippers. Given the observed trade-off between bending curvature and bending force, one could select either a taper angle that places a premium on bending curvature or bending force or a taper angle that balances both at moderate levels. In this study, we chose: (1) an intermediate taper angle ($\alpha = 9°$) that leads to a good balance between high force application and moderate bending curvature and (2) a relatively small taper angle ($\alpha = 4.5°$) that places a premium on bending curvature over applied bending force (attachment force of the $\alpha = 4.5°$ gripper against different surfaces is provided in Supplementary Fig. S18).

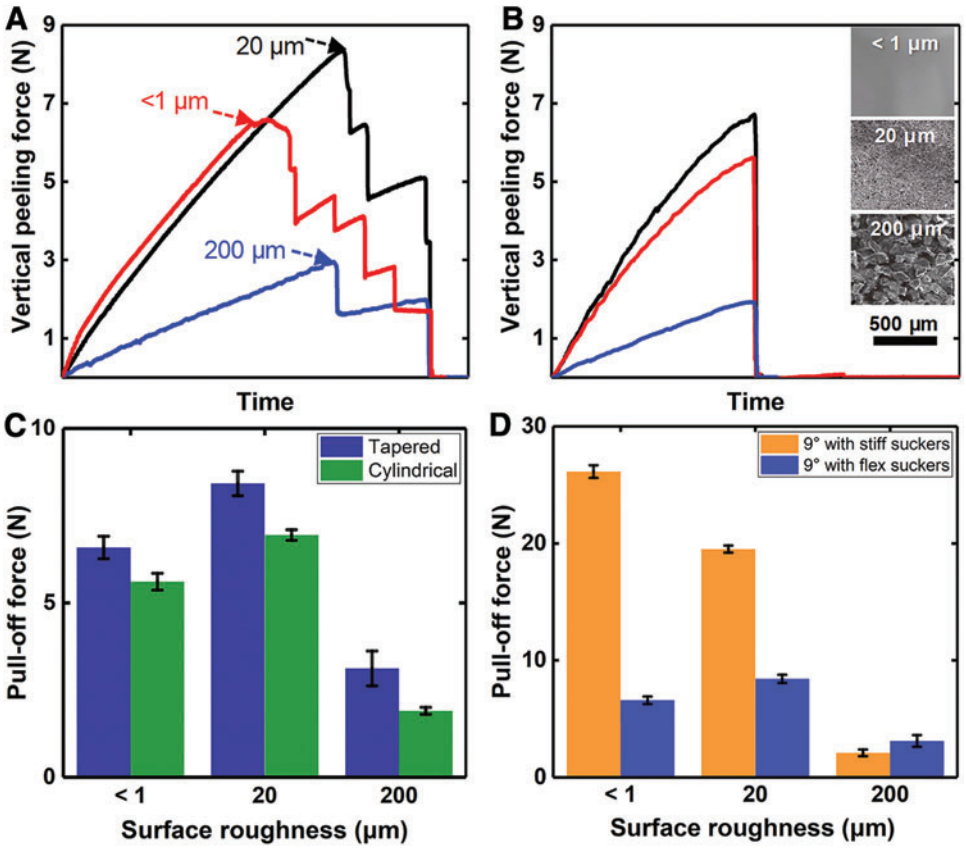

FIG. 5. Attachment force of the $\alpha = 9°$ tapered gripper and its corresponding cylindrical gripper against different surfaces. Soft sucker (Young's modulus: 260 kPa) vertical peeling forces plotted against time for surfaces of various roughnesses (R_a: <1, 20, 200 μm) for **(A)** the $\alpha = 9°$ tapered gripper and **(B)** its corresponding cylindrical gripper, demonstrating the stair step-like failure mode of the tapered actuator **(A)**. The corresponding scanning electron microscopic images for the different surfaces are shown in **(B**, *inset*). **(C)** The attachment forces of the $\alpha = 9°$ gripper and its corresponding cylindrical gripper on planar surfaces of various roughnesses (R_a: <1, 20, 200 μm). **(D)** The attachment forces of the $\alpha = 9°$ gripper with stiff (Young's modulus: 660 kPa) and flexible suckers (Young's modulus: 260 kPa) on planar surfaces of various roughnesses (R_a: <1, 20, 200 μm). Color images are available online.

Downloaded by Harvard University FRANCIS A COUNTWAY from www.liebertpub.com at 02/28/20. For personal use only.

We first demonstrated the abilities of our tapered grippers to attach, wrap, transport, and deliver an object of interest, which necessitated the use of both bending and suction functionalities (Fig. 6A). Specifically, a thin plastic sheet was grasped from an initially planar geometry and then transported and delivered in a rolled-up orientation—an operation that could be useful in assembly line applications involving thin membranes. In this example, the gripper characterized by $\alpha = 4.5°$ was able to move the thin sheet in three steps (Fig. 6A and Supplementary Movie S3): (1) starting with the nonpressurized gripper (0 s), the suction cups made contact with the planar surface and a vacuum was applied. (2) Once the system detected the pressure change from the suckers, the robotic arm lifted the sheet to a predefined height above the workspace (4 s). At ~6 s (a preset time delay), the gripper was then pressurized ($P = 250$ kPa) to ''wrap'' the sheet into a roll (6.5 s). (3) The robotic arm transported the sheet quickly (8 s) and at a constant speed and then delivered it to a human hand at 12 s (by releasing the vacuum and inflation pressure). Supplementary Figure S20 shows the inflation and vacuum pressures as a function of time during this process. Based on the pressure sensory feedback, the ''attach, wrap, transport, and deliver'' motion could be utilized in a semiautonomous way and could achieve safe and efficient assistance when interacting with a human subject. We also want to point out that we repeated the ''attach, wrap, transport, and deliver'' experiment 20 times and observed a 100% success rate, demonstrating the robustness of our system. Similar results were also observed with the $\alpha = 9°$ gripper, but the wrapping abilities were reduced based on the actuator's larger taper angle leading to smaller curvatures (Supplementary Movie S5).

To further expand on the practical applications of our design, we sought to create a seamless human–machine interface to control pressurization and depressurization. As an initial proof of concept, we constructed a device that integrated a pressurization valve and vacuum generator into a bulb-shaped handle (60 mm in diameter), with two buttons operable by a single human hand (Fig. 6B). Using this bulb-shaped handle, we then examined the prototype's ability to grasp common objects (Fig. 6C). Both the $\alpha = 4.5°$ and the $\alpha = 9°$ handheld prototypes

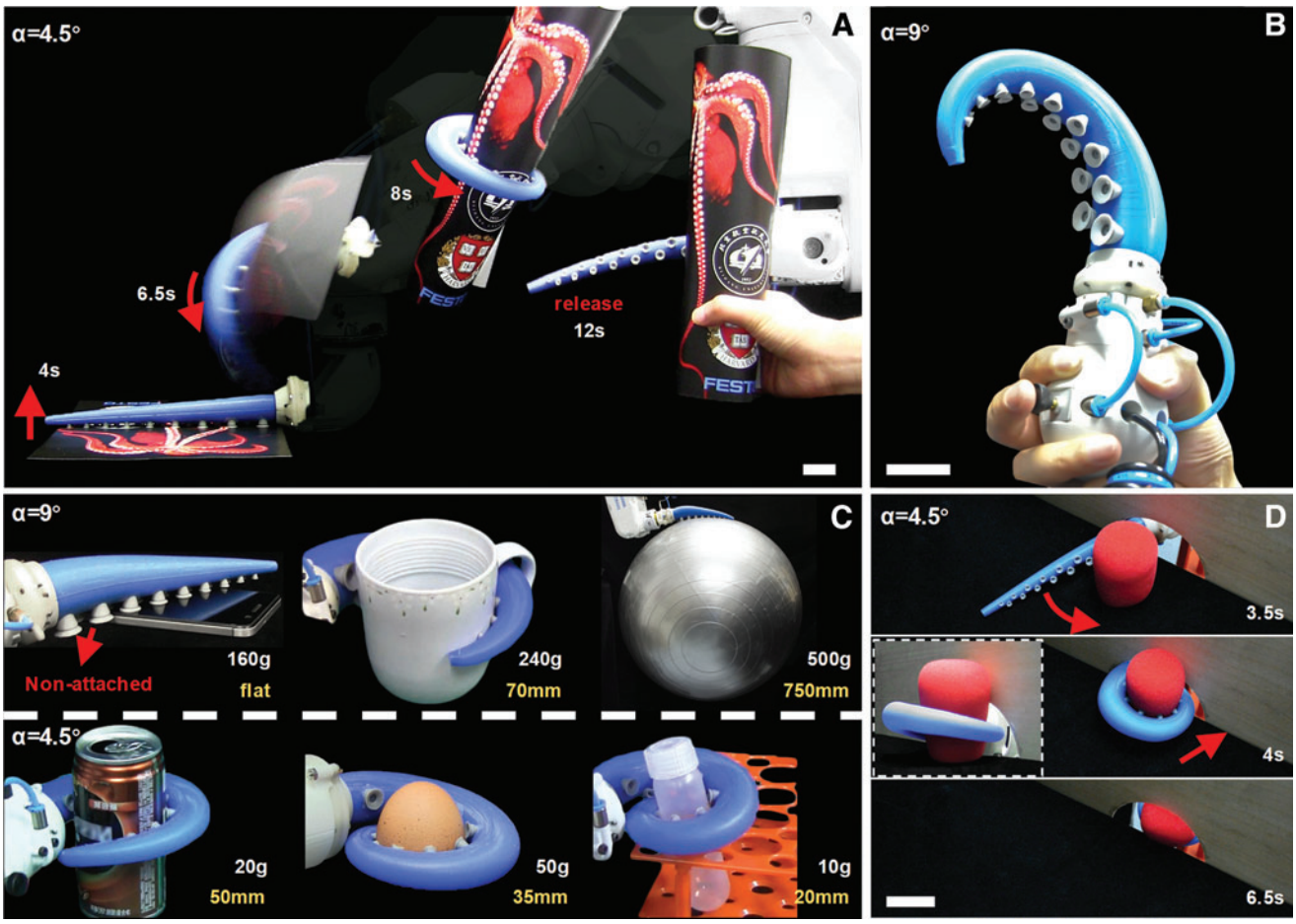

FIG. 6. Exploring the application space for the tapered grippers. **(A)** Suction and bending for picking up, rolling, and placing a printed plastic sheet (see Supplementary Fig. S20 for details of its pressure control). This specific task is termed ''attach, wrap, transport, and deliver''—a video of which is available in Supplementary Movie S3 (scale bar, 30 mm). **(B)** In a modified configuration, a two-button bulb-like controller that integrates a pressure valve and vacuum regulator is used, allowing for simple, one-hand operability (scale bar, 30 mm). **(C)** The tapered grippers can grip a wide range of objects via this handheld controller. *Upper row*: $\alpha = 9°$ gripper; *lower row*: $\alpha = 4.5°$ gripper. Video documentation of these actions are provided in Supplementary Movies S4 and S5. The weights and sizes of the objects are indicated for each grasped object. **(D)** The tapered gripper retrieving objects from confined spaces—a video of which is available in Supplementary Movie S8 (scale bar, 30 mm). Color images are available online.

Downloaded by Harvard University FRANCIS A COUNTWAY from www.liebertpub.com at 02/28/20. For personal use only.

were able to adequately grasp objects, such as a test tube (with a diameter of 20 mm), a mug (with a diameter of 70 mm), or a yoga ball (with a diameter of 750 mm); however, each actuator clearly has its strengths and weaknesses based on the previously observed trade-offs between curvature and applied bending force. The tapered gripper with $\alpha = 4.5°$, for example, was able to more easily grasp the light weight items with higher curvatures, such as the can, egg, and test tube, whereas the $\alpha = 9°$ gripper struggled to do so (Fig. 6C and Supplementary Movies S4 and S5). This observation is due to the fact that the actuator with $\alpha = 4.5°$ can bend into a larger curved state (a spiral shape with the tip of the actuator curling past its base) than the actuator with $\alpha = 9°$ (Supplementary Fig. S21A and Supplementary Movies S6 and S7). However, the $\alpha = 9°$ gripper was able to more easily grasp the heavier and bulkier objects with lower curvatures, such as the mug and yoga ball (Fig. 6C), and a bucket of water weighing up to 27 N, which is over 24 times the weight of the gripper (Supplementary Fig. S21B). Moreover, the $\alpha = 9°$ gripper was capable of gripping a cell phone even when some of the suction cups are nonattached to the surface (Fig. 6C). These results confirm that the combination of bending (with choosing the appropriate taper angle) and suction can allow for the grasping of an extremely wide range of objects, including planar and nonplanar geometries, rigid and soft, and rough and smooth objects.

Since octopuses are well known for the ability to retrieve objects from confined spaces by adaptively deforming the arm when going through/out a small opening,[48] we also investigated whether our octopus-inspired actuator with suckers could perform similar functions. To carry out these studies, we considered a wall with a 4 cm diameter hole and then placed a deformable object measuring 8 cm in height on one side (Fig. 6D) and the $\alpha = 4.5°$ gripper (which was barely small enough to fit through the opening) connected to a robotic arm (MOTOMAN MH3F; YASKAWA, Inc., Japan) on the other side (Supplementary Movie S8). The enhanced flexibility provided by the tapered design enabled the gripper to extend almost its entire length through the opening (3.5 s), to fetch a squishy object (4 s), and to return through the small opening with the object (6.5 s). The successful demonstration of this retrieving behavior was only possible with our streamlined tapered design and thus highlights the further usefulness of this conical geometry for object manipulation in constrained environments. We also mounted the gripper on an elephant trunk-like (or octopus arm-like) appendage (Supplementary Movie S9) to demonstrate a large-scale continuum of motion in three-dimensional space that could be safely operated in the company of human bystanders.

Conclusions

In the present report, we used a combination of numerical analyses and experiments to investigate the response of tapered octopus-inspired soft actuators. We found that, in contrast to typical soft actuators with a cylindrical shape that bend with a constant curvature,[24,27–31] the tapered actuators considered in this study could achieve nonconstant bending curvature along their lengths and a more spiral-like shape (Supplementary Fig. S22). Guided by the numerical analyses, we then designed and fabricated a multifunctional tapered gripper and evaluated its gripping ability over a wide range of structurally diverse objects. Importantly, we found that the enhanced flexibility of the tapered design translated into higher gripping power. Surprisingly, through the combined action of bending and suction, our tapered gripper could easily grip a variety of flat, curved, smooth, and rough items, ranging in diameter from 5 mm (Fig. 1H) to 750 mm (Fig. 6C) and weights up to 27 N (Supplementary Fig. S21B). The varying bending curvature along the length is an intriguing and potentially useful phenomenon in that it enables gripping of objects of significantly smaller sizes than those typically manipulated employing a nontapered geometry.

The pneumatic pressure input (and the resulting bending curvature) was also seen to play an important role in the interfacial attachment of the suckers to nonplanar surfaces and could thus be employed to maximize the attachment performance of the suckers to such surfaces. As a result, and in contrast to previously documented soft actuators employing other mechanisms of biologically inspired adhesion,[49–52] our tapered actuators with suckers can easily grip a variety of flat, curved, smooth, and rough items through the combined action of bending and suction. Compared with grippers that require several actuators organized into a hand-like geometry,[27,33,34,37,53] our system requires only a single actuator to complete tasks thanks to its tapered form and combined bending and suction features. This streamlined, high aspect ratio, multifunctional architecture thus enables the actuators to perform tasks in narrow and constrained conditions (Fig. 6D and Supplementary Movie S8), behaviors that are functionally similar to those observed in living octopus.[48]

While in this study, our actuators' designs mimic only the bending motion of an octopus arm, future prototypes could also incorporate three-dimensional (out of plane) bending and elongation,[54,55] material stiffness variability,[56–58] more structurally complex biomimetic suckers,[42,46] or the incorporation of reinforcing fibrous components[29,31] for added functionality. Additionally, the overall gripping performance of the actuators could be significantly enhanced by optimizing the sucker size and pattern for different arm taper angles. In the current study, because of the compact design of the actuators, we employed a simplified vacuum system to actuate the suckers, but we imagine that the *acetabular* contraction of the suckers could be more closely mimicked in future studies with different types of soft actuators, including those based on dielectric elastomers,[59,60] shape memory polymers,[61] or hydrogels.[40,62,63] It should also be noted that the arm's taper angle can be dynamically altered in living octopuses when catching prey items of different sizes or weights[64] and could, in theory, be replicated in our soft robotic analogs using some of the design strategies and materials systems outlined above. The results and diverse octopus-inspired design elements described here could thus help lay the foundation for the future design of dynamically morphable soft robots that can adapt in real time to perform specific tasks of interest.

Finally, our results also have implications for understanding the biomechanics of octopus arms. In nature, an octopus with a small arm taper angle (e.g., *O. macropus*, $3.58° \pm 0.33°$), and with a correspondingly thinner muscular structure, produces smaller bending radii to catch small preys compared with an octopus with a larger arm taper angle (e.g., *E. cirrhosa*, $9.32° \pm 1.66°$) with a thicker muscular structure.[65] The ecological and evolutionary consequences of this variability may be related to (1) size, strength, and speed of potential prey items, (2) habitat structural heterogeneity, or

(3) depth-dependent food availability and related octopus energetics. While the precise reasons for this observed diversity of arm taper angle are still largely unknown, the results reported here may shed new light on this matter and may stimulate further hypothesis testing into the various possibilities outlined above.

Acknowledgment

We would like to thank William Kier, Paul Valentich-Scott, and Eric Hochberg for helpful suggestions.

Author Disclosure Statement

L.W., Z.X., E.M.K., and Z.G. are inventors on the patent application (CN201710346369.1) submitted by Beihang University that covers the structure design of the tentacle gripper.

Funding Information

This work was supported by the National Science Foundation support projects, China (grant nos. 61822303, 61633004, 91848105 to L.W.) and the National Key Research and Development Program of China (no. 2018YFB1304604). K.B. gratefully acknowledges support by the National Science Foundation through grant DMREF-1533985 and the Wyss Institute for Biologically Inspired Engineering. Z.X. thanks the Innovation Foundation project YCSJ-03-2018-03 of Beihang University for PhD Graduates. Special thanks to Festo Corporate project for the financial support of the prototype development in the early stage.

Supplementary Material

Supplementary Data
Supplementary Movie S1
Supplementary Movie S2
Supplementary Movie S3
Supplementary Movie S4
Supplementary Movie S5
Supplementary Movie S6
Supplementary Movie S7
Supplementary Movie S8
Supplementary Movie S9

References

1. Laschi C, Mazzolai B, Cianchetti M. Soft robotics: technologies and systems pushing the boundaries of robot abilities. Sci Robot 2016;1:eaah3690.
2. Pfeifer R, Lungarella M, Iida F. Self-organization, embodiment, and biologically inspired robotics. Science 2007; 318:1088–1093.
3. Ijspeert AJ. Biorobotics: using robots to emulate and investigate agile locomotion. Science 2014;346:196–203.
4. Kizilkan E, Strueben J, Staubitz A, *et al.* Bioinspired photocontrollable microstructured transport device. Sci Robot 2017;2:eaak9454.
5. Koh JS, Yang E, Jung GP, *et al.* Jumping on water: surface tension-dominated jumping of water striders and robotic insects. Science 2015;349:517–521.
6. Wen L, Weaver JC, Lauder GV. Biomimetic shark skin: design, fabrication and hydrodynamic function. J Exp Biol 2014;217:1656–1666.
7. Wang Y, Yang X, Chen Y, *et al.* A biorobotic adhesive disc for underwater hitchhiking inspired by the remora suckerfish. Sci Robot 2017;2:eaan8072.
8. Domel AG, Saadat M, Weaver JC, *et al.* Shark skin-inspired designs that improve aerodynamic performance. J R Soc Interface 2018;15:20170828.
9. Vail AL, Manica A, Bshary R. Referential gestures in fish collaborative hunting. Nat Commun 2013;4:1765.
10. Richter JN, Hochner B, Kuba MJ. Octopus arm movements under constrained conditions: adaptation, modification and plasticity of motor primitives. J Exp Biol 2015;218:1069–1076.
11. Smith A. Cephalopod sucker design and the physical limits to negative pressure. J Exp Biol 1996;199:949–958.
12. Sumbre G, Gutfreund Y, Fiorito G, *et al.* Control of octopus arm extension by a peripheral motor program. Science 2001;293:1845–1848.
13. Margheri L, Laschi C, Mazzolai B. Soft robotic arm inspired by the octopus: I. From biological functions to artificial requirements. Bioinspir Biomim 2012;7:025004.
14. Laschi C, Mazzolai B. Lessons from animals and plants: the symbiosis of morphological computation and soft robotics. IEEE Robot Automat Mag 2016;23:107–114.
15. Calisti M, Giorelli M, Levy G, *et al.* An octopus-bioinspired solution to movement and manipulation for soft robots. Bioinspir Biomim 2011;6:036002.
16. Mazzolai B, Margheri L, Cianchetti M, *et al.* Soft-robotic arm inspired by the octopus: II. From artificial requirements to innovative technological solutions. Bioinspir Biomim 2012;7:025005.
17. Laschi C, Cianchetti M, Mazzolai B, *et al.* Soft robot arm inspired by the octopus. Adv Robot 2012;26:709–727.
18. Renda F, Cianchetti M, Giorelli M, *et al.* A 3D steady-state model of a tendon-driven continuum soft manipulator inspired by the octopus arm. Bioinspir Biomim 2012;7: 025006.
19. Giorelli M, Renda F, Calisti M, *et al.* Learning the inverse kinetics of an octopus-like manipulator in three-dimensional space. Bioinspir Biomim 2015;10:035006.
20. Grissom MD, Chitrakaran V, Dienno D, *et al.* Design and experimental testing of the octarm soft robot manipulator (Unmanned Systems Technology VIII, vol. 6230). Orlando, FL: International Society for Optics and Photonics, 2006, p. 62301F.
21. Walker ID, Dawson DM, Flash T, *et al.* Continuum robot arms inspired by cephalopods (Unmanned Ground Vehicle Technology VII, vol. 5804). Orlando, FL: International Society for Optics and Photonics, 2005, pp. 303–315.
22. Cianchetti M, Calisti M, Margheri L, *et al.* Bioinspired locomotion and grasping in water: the soft eight-arm OCTOPUS robot. Bioinspir Biomim 2015;10:035003.
23. Katzschmann RK, Marchese AD, Rus D. Autonomous object manipulation using a soft planar grasping manipulator. Soft Robot 2015;2:155–164.
24. Marchese AD, Rus D. Design, kinematics, and control of a soft spatial fluidic elastomer manipulator. Int J Robot Res 2016;35:840–869.
25. Rus D, Tolley MT. Design, fabrication and control of soft robots. Nature 2015;521:467.
26. Majidi C. Soft robotics: a perspective—current trends and prospects for the future. Soft Robot 2014;1:5–11.
27. Shepherd RF, Stokes AA, Nunes RMD, *et al.* Soft machines that are resistant to puncture and that self seal. Adv Mater 2013;25:6709–6713.

Downloaded by Harvard University FRANCIS A COUNTWAY from www.liebertpub.com at 02/28/20. For personal use only.

Downloaded by Harvard University FRANCIS A COUNTWAY from www.liebertpub.com at 02/28/20. For personal use only.

28. Mosadegh B, Polygerinos P, Keplinger C, *et al.* Pneumatic networks for soft robotics that actuate rapidly. Adv Funct Mater 2014;24:2163–2170.
29. Polygerinos P, Wang Z, Overvelde JTB, *et al.* Modeling of soft fiber-reinforced bending actuators. IEEE Trans Robot 2015;31:778–789.
30. Ranzani T, Gerboni G, Cianchetti M, *et al.* A bioinspired soft manipulator for minimally invasive surgery. Bioinspir Biomim 2015;10:035008.
31. Connolly F, Walsh CJ, Bertoldi K. Automatic design of fiber-reinforced soft actuators for trajectory matching. Proc Natl Acad Sci 2017;114:51–56.
32. Kwok SW, Morin SA, Mosadegh B, *et al.* Magnetic assembly of soft robots with hard components. Adv Funct Mater 2014;24:2180–2187.
33. Deimel R, Brock O. A novel type of compliant and underactuated robotic hand for dexterous grasping. Int J Robot Res 2016;35:161–185.
34. Shepherd RF, Ilievski F, Choi W, *et al.* Multigait soft robot. Proc Natl Acad Sci 2011;108:20400–20403.
35. Terryn S, Brancart J, Lefeber D, *et al.* Self-healing soft pneumatic robots. Sci Robot 2017;2:eaan4268.
36. Brojan M, Videnic T, Kosel F. Large deflections of nonlinearly elastic non-prismatic cantilever beams made from materials obeying the generalized Ludwick constitutive law[J]. Meccanica 2009;44:733–739.
37. Baik S, Park Y, Lee T J, *et al.* A wet-tolerant adhesive patch inspired by protuberances in suction cups of octopi. Nature 2017;546:396.
38. Hou J, Wright E, Bonser RHC, *et al.* Development of biomimetic squid-inspired suckers. J Bionic Eng 2012;9:484–493.
39. Choi MK, Park OK, Choi C, *et al.* Cephalopod-inspired miniaturized suction cups for smart medical skin. Adv Health Mater 2016;5:80–87.
40. Lee H, Um DS, Lee Y, *et al.* Octopus-inspired smart adhesive pads for transfer printing of semiconducting nanomembranes. Adv Mater 2016;28:7457–7465.
41. Lucas KN, Johnson N, Beaulieu WT, *et al.* Bending rules for animal propulsion. Nat Comm 2014;5:3293.
42. Tramacere F, Beccai L, Kuba MJ, *et al.* Octopus suckers identification code (OSIC). Mar Freshw Behav Physiol 2013;46:447–453.
43. Kier WM, Smith AM. The morphology and mechanics of octopus suckers. Biol Bullet 1990;178:126–136.
44. Kier WM, Smith AM. The structure and adhesive mechanism of octopus suckers. Integr Comp Biol 2002;42:1146–1153.
45. Gent AN. A new constitutive relation for rubber. Rub Chem Tech 1996;69:59–61.
46. Tramacere F, Follador M, Pugno NM, *et al.* Octopus-like suction cups: from natural to artificial solutions. Bioinspir Biomim 2015;10:035004.
47. Han JY. Low-cost multi-touch sensing through frustrated total internal reflection. In: Proceedings of the 18th Annual ACM Symposium on User Interface Software and Technology. ACM, 2005, pp. 115–118.
48. Caldwell RL, Ross R, Rodaniche A, *et al.* Behavior and body patterns of the larger Pacific striped octopus. PloS One 2015; 10:e0134152.
49. Autumn K, Liang YA, Hsieh ST, *et al.* Adhesive force of a single gecko foot-hair. Nature 2000;405:681.
50. Song S, Drotlef DM, Majidi C, *et al.* Controllable load sharing for soft adhesive interfaces on three-dimensional surfaces. Proc Natl Acad Sci 2017;114:E4344–E4353.
51. Glick P, Suresh SA, Ruffatto D, *et al.* A soft robotic gripper with gecko-inspired adhesive. IEEE Robot Autom Lett 2018;3:903–910.
52. Li J, Celiz AD, Yang J, *et al.* Tough adhesives for diverse wet surfaces. Science 2017;357:378–381.
53. Hao Y, Gong Z, Xie Z, *et al.* Universal soft pneumatic robotic gripper with variable effective length. In: 2016 35th Chinese Control Conference (CCC). IEEE 2016, pp. 6109–6114.
54. Robertson MA, Paik J. New soft robots really suck: vacuum-powered systems empower diverse capabilities. Sci Robot 2017;2:eaan6357.
55. Kim SJ, Lee DY, Jung GP, *et al.* An origami-inspired, self-locking robotic arm that can be folded flat. Sci Robot 2018; 3:eaar2915.
56. Bartlett NW, Tolley MT, Overvelde JTB, *et al.* A 3D-printed, functionally graded soft robot powered by combustion. Science 2015;349:161–165.
57. Elsayed Y, Vincensi A, Lekakou C, *et al.* Finite element analysis and design optimization of a pneumatically actuating silicone module for robotic surgery applications. Soft Robot 2014;1:255–262.
58. Lekakou C, Elsayed Y, Geng T, *et al.* Skins and sleeves for soft robotics: inspiration from nature and architecture. Adv Eng Mater 2015;17:1180–1188.
59. Shian S, Bertoldi K, Clarke DR. Dielectric elastomer based ''grippers'' for soft robotics. Adv Mater 2015;27:6814–6819.
60. Shintake J, Rosset S, Schubert B, *et al.* Versatile soft grippers with intrinsic electroadhesion based on multifunctional polymer actuators. Adv Mater 2016;28:231–238.
61. Zhao Z, Zhang K, Liu Y, *et al.* Highly stretchable, shape memory organohydrogels using phase-transition microinclusions. Adv Mater 2017;29:1701695.
62. Fu F, Shang L, Chen Z, *et al.* Bioinspired living structural color hydrogels. Sci Robot 2018;3:eaar8580.
63. Kim YS, Liu M, Ishida Y, *et al.* Thermoresponsive actuation enabled by permittivity switching in an electrostatically anisotropic hydrogel. Nat Mater 2015;14:1002.
64. Kier WM, Stella MP. The arrangement and function of octopus arm musculature and connective tissue. J Morphol 2007;268:831–843.
65. Steer MA, Semmens JM. Pulling or drilling, does size or species matter? An experimental study of prey handling in *Octopus dierythraeus*. J Exp Marine Biol Ecol 2003;290:165–178.

Address correspondence to:
Li Wen
School of Mechanical Engineering and Automation
Beihang University
Beijing 100083
China

E-mail: liwen@buaa.edu.cn

Katia Bertoldi
John A. Paulson School of Engineering
and Applied Sciences
Harvard University
Cambridge, MA 02138

E-mail: bertoldi@seas.harvard.edu

Supplementary materials for

Octopus arm-inspired tapered soft actuators with suckers for improved grasping

Zhexin Xie,[1,5‡] August G. Domel,[2‡] Ning An,[2] Connor Green,[2] Zheyuan Gong,[1] Tianmiao Wang,[1] Elias M. Knubben,[3] James C. Weaver,[4] Katia Bertoldi,[2*] Li Wen,[1*]

* Authors for correspondence: liwen@buaa.edu.cn and bertoldi@seas.harvard.edu
‡ These authors contributed equally to this work.

This file includes:

Supplementary Text
Fig. S1. Images of ten species of octopus for taper angles measurements.
Fig. S2. The sensitivity of the measurements to image deviations.
Fig. S3. Geometry of the tapered soft actuator.
Fig. S4. Design details of the soft suckers of tapered gripper.
Fig. S5. Design details of the soft suckers of cylindrical gripper.
Fig. S6. Fabrication of the tapered soft actuator.
Fig. S7. Tapered soft actuators.
Fig. S8. Material behavior.
Fig. S9. Curvature (α = 10.5° tapered actuator).
Fig. S10. Experimental results of bending curvature for α = 6° and α = 10.5° tapered actuators.
Fig. S11. Experimental results of bending force measurements.
Fig. S12. Comparisons between numerical and experimental results for the bending curvature of the α = 6° and α = 10.5° actuators.
Fig. S13. Simulation results of bending curvature of the tapered soft actuators.
Fig. S14. Comparisons between the numerical and experimental bending forces.
Fig. S15. Fabrication process of the tapered soft actuator with suckers.
Fig. S16. Two tapered grippers with taper angle α = 4.5° and α = 9°.
Fig. S17. Bending comparisons between actuators with suckers and without suckers at P = 200 kPa.
Fig. S18. Attachment force of the α = 4.5° gripper against different surfaces.
Fig. S19. Sucker attachment force measurements of the cylindrical actuator with suckers that of the same size and spatial distribution as those from the tapered actuator.

Fig. S20. The inflation and vacuum pressures as a function of time during the “attach, wrap, transport, and deliver” process.
Fig. S21. Motion of α = 4.5° and α = 9° grippers and load capability of α = 9° gripper.
Fig. S22. Bending comparisons: tapered and cylindrical soft actuator.
Table S1. Taper angles of biological octopus arms.
Movie S1. Side view of the peeling process of the α = 9° tapered gripper and its corresponded cylindrical gripper from a flat surface.
Movie S2. Suckers of the α = 9° tapered gripper and its corresponded cylindrical gripper attaching to and detaching from a translucent acrylic plate.
Movie S3. α = 4.5° gripper attaching to and rolling a flexible plastic sheet.
Movie S4. Gripping demonstration of the α = 4.5° gripper.
Movie S5. Gripping demonstration of the α = 9° gripper.
Movie S6. Motion of the α = 4.5° gripper.
Movie S7. Motion of the α = 9° gripper.
Movie S8. α = 4.5° gripper gripping demo through a narrow hole.
Movie S9. The tapered gripper mounted on an elephant-trunk-like robotic-arm for continuous motion.
Supplementary References (*41, 46, 58, 67*)

SUPPORTING INFORMATION

S1. Measuring the taper angles of octopus arms

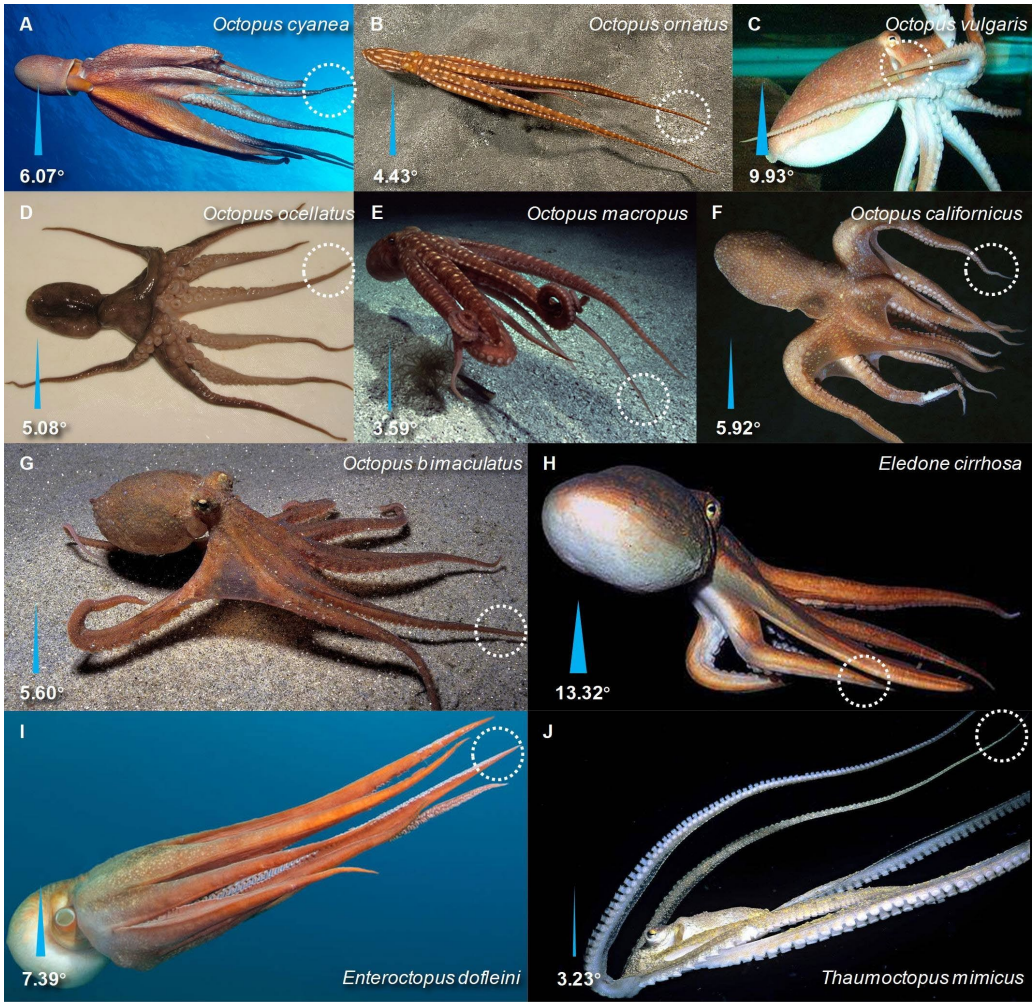

Fig. S1. Images of ten species of octopus for taper angles measurements. (A)-(J) Average arm taper angles for *Octopus cyanea* (6.07°), *Octopus ornatus* (4.43°), *Octopus vulgaris* (9.93°), *Octopus ocellatus* (5.08°), *Octopus macropus* (3.59°), *Octopus californicus* (5.92°), *Octopus bimaculatus* (5.60°), *Eledone cirrhosa* (13.32°), *Enteroctopus dofleini* (7.39°), and *Thaumoctopus mimicus* (3.23°).

Table S1. Taper angles of biological octopus arms.

Octopus species	Taper angles α (°)						
Octopus cyanea	5.55	6.07	6.12	6.66			
Octopus ornatus	4.01	4.43					
Octopus vulgaris	5.51	5.61	6.83	6.86	7.21	9.37	9.93
Octopus ocellatus	4.18	5.08					
Octopus macropus	3.01	3.59	4.14				
Octopus californicus	5.92	7.03					
Octopus bimaculatus	4.89	5.60	5.91				
Eledone cirrhosa	6.25	6.95	10.76	13.32			
Enteroctopus dofleini	7.39	7.78	9.63				
Thaumoctopus mimicus	2.95	3.23	6.31				

It should be noted that a similar measurement method (from online images and videos) was recently used for studying the flexion morphospace of wings/fins among different animals species (*41*). Furthermore, to confirm the validity of our approach, we evaluated the sensitivity of the measurements to image deviations. To this end, we calculated the measurement error e_α as:

$$e_\alpha = \frac{\alpha_p - \alpha_r}{\alpha_r} \quad [1]$$

where α_p is the taper angle measured from the image and α_r is the real taper angle, which is given by

$$tan\frac{\alpha_r}{2} = tan\frac{\alpha_p}{2} cos\tau, \quad [2]$$

with τ denoting the perspective angle deviation (see Fig. S2). We found that for reasonable perspective angle deviations (τ < 30°) , e_α =15.5% for *Thaumoctopus mimicus* (for which we measured α =2.95°) and e_α =15.3% for *Eledone cirrhosa* (for which we measured α =13.32°). As such, we can conclude that these potential measurement errors do not alter the conclusion that the octopus taper angle varies among different species.

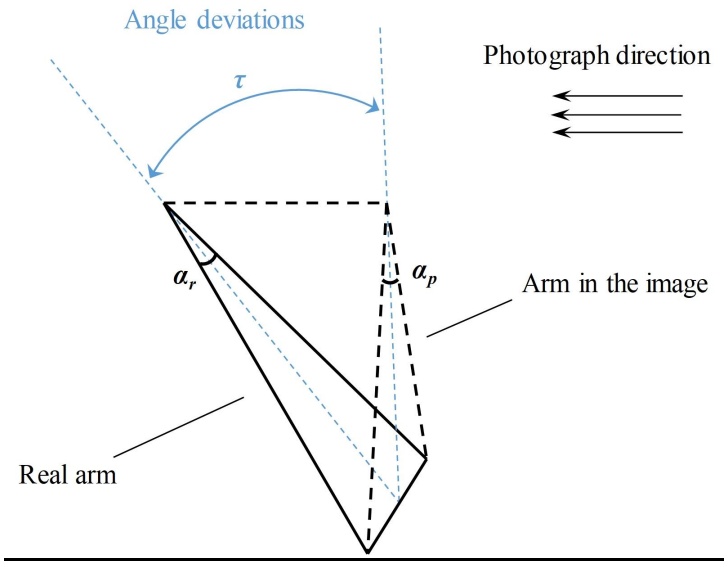

Fig. S2. The sensitivity of the measurements to image deviations. Schematic illustrating α_p, α_r and τ.

S2. Geometry of the soft actuators and their suckers

As shown in Fig. S3A, the actuators considered in this study are cone-shaped with a taper angle α, length L = 200 *mm* and tip radius R_{tip} = 4.2 mm. As such, the outer radius $R_o(z)$ and cross sectional area $S_o(z)$ of the actuator at a distance z ($0 < z < L$) from the tip is given by

$$R_o(z) = R_{tip} + z\tan\frac{\alpha}{2} \quad [3]$$

and

$$S_o(z) = \pi R_o(z)^2. \quad [4]$$

A single inner pneumatic chamber running the length of the actuator was used as a simple, effective way to induce bending in the actuator (*58*, *67*). This chamber has a β = 120° swept cross-section, an outer radius $R_i(z)$, *and* an inner radius $R_m(z)$ (see cross-section in Fig. S3A). The chamber was placed at a fixed normalized distance from the outer radius of the actuator; specifically, the chamber placement was defined so that

$$\frac{R_o(z)}{R_o(z)-R_i(z)} = K\,, \quad [5]$$

where K denotes a constant that determines the placement of the chamber cross-section with respect to the edge of the actuator's cross-section (see Fig. S3B). Note that by varying K, we can study how the normalized distance from the outside of the chamber to the outside of the actuator affects the bending of the actuator. It follows from Eq. **5** that the chamber's outer radius, $R_i(z)$, at a distance z from the tip is given by

$$R_i(z) = \frac{K-1}{K}R_o(z). \quad [6]$$

Moreover, the ratio of the cross-sectional area of the inner chamber, $S_i(z)$, to the cross-sectional area of the actuator, $S_o(z)$, was kept constant along the length

$$\frac{S_i(z)}{S_o(z)} = 0.05. \quad [7]$$

It follows that to satisfy Eq. **7** the inner radius of the chamber $R_m(z)$ is given by

$$R_m(z) = \sqrt{R_o(z)^2 - \frac{0.05\, S_0(z)}{\pi}}. \quad [8]$$

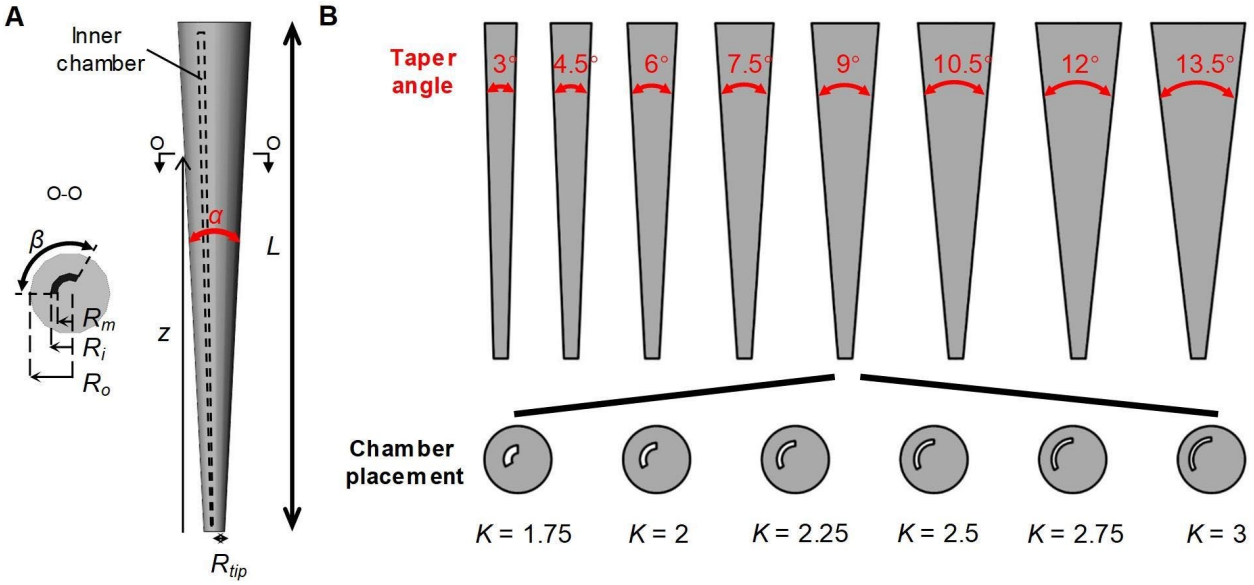

Fig. S3. Geometry of the tapered soft actuator. (A) Cross-sectional view and side view of the actuator with a arch-shaped inner chamber for pressurization. The actuator length (L), taper angle (α), outer radius (R_o), chamber outer radius (R_i), and chamber inner radius (R_m) are indicated in the image. **(B)** 8 actuators of different taper angles (α from 3° to 13.5° with an interval of 1.5°, K = 2) and 6 actuator of different chamber placements (K from 1.75 to 3 with an interval of 0.25, α = 9°) were considered in this study.

To improve the grasping ability of these tapered actuators, we next integrated suckers into their design. The shape of our suckers mimic that of the *infundibulum* and *acetabulum* of *Octopus vulgaris* (see Fig. S4A). Specifically, for the *j-th* sucker with outer diameter d_j, we choose the *infundibulum* height, e_j, and inner diameter, f_j, (Figs. 4A-E) as

$$e_j = \frac{d_j}{4} \quad [9]$$

and

$$f_j = \frac{d_j}{2}. \quad [10]$$

Moreover, as Fig. S4G shows, the sucker's diameter d_j is chosen to be

$$d_j = R_o(z_j). \quad [11]$$

where z_j denotes the location of the *j*-th sucker along the actuator.

Based on the octopus images we analyzed, we arranged 17 suckers (14 of which were connected to vacuum) with decreasing diameters in a staggered pattern along the tapered actuator (see Figs. S4E-G). While the non-vacuum actuated nature of the three smallest suckers was a necessity based on fabrication constraints, they still provided a small amount of adhesion force during initial object contact before and after the vacuum actuated suckers are fully engaged. The position of the center point for the *j-th* sucker (see black dot in Fig. 4F) is defined by coordinates z_j and x_j, which are given by

$$z_j = \begin{cases} L - \frac{5R_o(L)\cos\frac{\alpha}{2}}{4} & j = 1 \\ L + \frac{R_o(L)\cos\frac{\alpha}{2}}{100}j^2 - \frac{17R_o(L)\cos\frac{\alpha}{2}}{25}j - \frac{29R_o(L)\cos\frac{\alpha}{2}}{50} & j = 2,3,\dots,17 \end{cases} \quad [12]$$

and

$$x_j = R_{tip} + z_j tan\frac{\alpha}{2} + \frac{9R_o(L)}{25cos\frac{\alpha}{2}} - \frac{3R_o(L)}{200cos\frac{\alpha}{2}}j\,, \quad [13]$$

where $R_o(L)$ is the radius at the base of the actuator ($z = L$), which is defined by Eq. **5**

Finally, we also evaluated the potential performance benefits of the tapered shape over that of its its cylindrical counterpart. As shown in Fig. S5, this cylindrical gripper consists of a cylindrical actuator with 14 integrated (and identical) suckers. Specifically, the cylindrical actuator has radius ($\widetilde{R_o}$)identical to the base radius of the tapered gripper

$$\widetilde{R_o} = R_o(L), \quad [14]$$

and is actuated by a pneumatic chamber, which followed the same design rules as were used for the tapered gripper (and defined by Eq. 5). Moreover, the position of the center point for the *j-th* sucker on such cylindrical actuator (see black dot in Fig. 5B) is defined by coordinates $\widetilde{z_j}$ and $\widetilde{x_j}$, which are given by

$$\widetilde{z_j} = \begin{cases} z_j & j = 1 \\ z_j - \frac{3\widetilde{R_o}}{5}(j-1) & j = 2,3,\dots,14 \end{cases} \quad [15]$$

and

$$\widetilde{x_j} = \frac{67}{50}\widetilde{R_o}\,. \quad [16]$$

It should be noted that on the cylindrical gripper, all of the suckers have identical size and diameter $\tilde{d}$ chosen to provide the same suction areas as employed in the tapered gripper

$$14\tilde{d}^2 = \sum_1^{17} {d_j}^2, \quad [17]$$

where d_j is the diameter of the *j-th* suckers of the tapered gripper, which is defined by Eq. **11**.

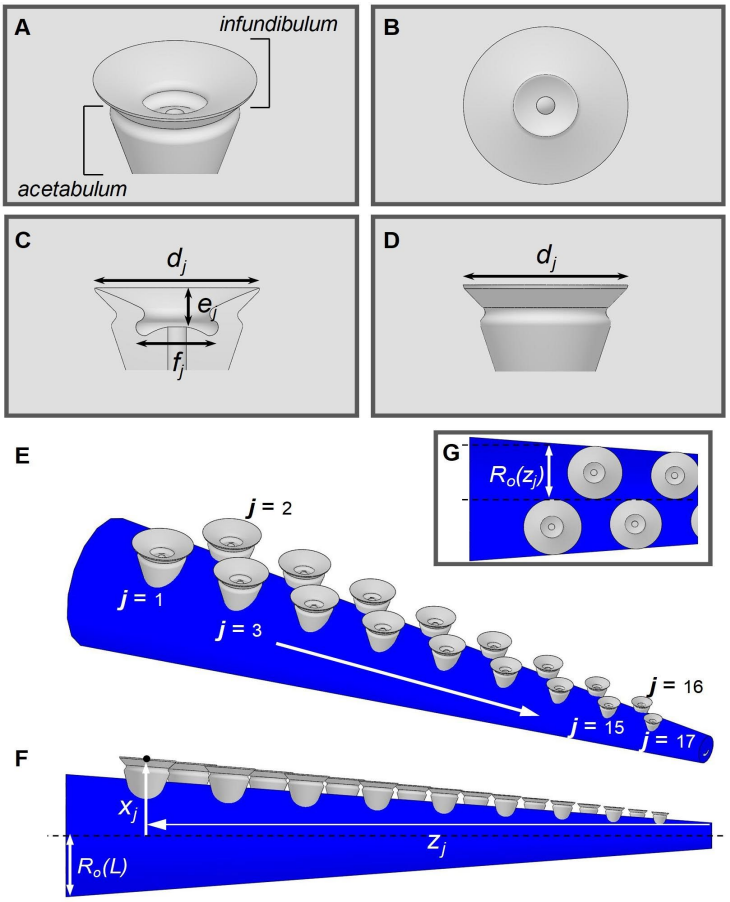

Fig. S4. Design details of the soft suckers of tapered gripper. (A) Isometric view, **(B)** top view, **(C)** cross sectional view and **(D)** side view of the sucker model with the corresponding design parameters. **(E)-(G)** Views of the tapered gripper with suckers arranged on its surface with a staggered distribution.

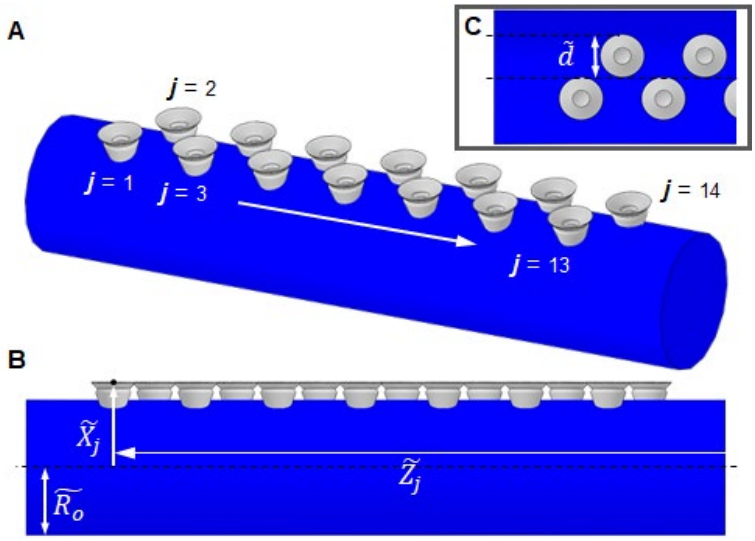

Fig. S5. Design details of the soft suckers of cylindrical gripper. (A)-(C) Views of the cylindrical gripper with identically sized suckers arranged on its surface. The cylindrical gripper has the same bottom diameter and curved inner chamber as its corresponding tapered gripper.

S3. Fabrication of tapered soft actuators without suckers and characterization of the material response

In order to validate the finite element simulations, we began by fabricating the tapered soft actuators (without suckers) for testing, which was performed using a molding and casting process (Fig. S6). All the molds were designed in SolidWorks and printed using a 3D printer (Makerbot Replicator X5, MakerBot Industries LLC, HK, China). The molds were assembled and held together firmly with tightly looped rubber rings while a 3D-printed rod with a β = 120° swept arch-shaped cross-section was positioned inside the tapered mold for the creation of the internal pneumatic chamber of the actuator. A 3D-printed cap was placed on top of the mold to hold the rod in place. A silicone elastomer with Young's modulus of E = 0.66 MPa (Mold Star 30, Smooth-On Inc., PA) was then poured into the mold (Fig. S6A), and degassed in a vacuum chamber for ten minutes. The elastomer was then left for 6 hours at room temperature to cure. After curing, the tapered mold and rod were removed, which created a core used for the actuator's inner pneumatic chamber. Finally, the actuator was sealed with adhesives (Sil-Poxy, Smooth-On Inc., PA) (Fig. S6B).

For this study, we fabricated eight actuators, all characterized by K=2 and with α = 3°, 4.5°, 6°, 7.5°, 9°, 10.5°, 12°, and 13.5° (Fig. S7), which were used to experimentally measure bending curvature and bending force for the purpose of validating the simulations.

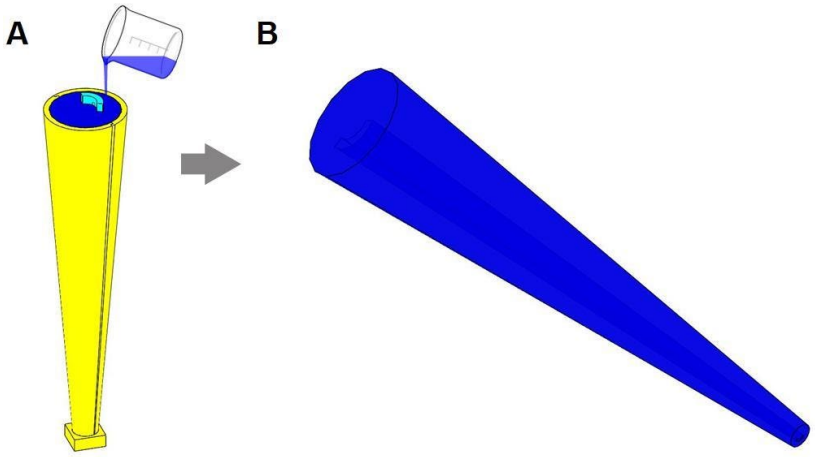

Fig. S6. Fabrication of the tapered soft actuator. (A) 3D-printed molds were used to cast the actuators. **(B)** The cured tapered soft actuator.

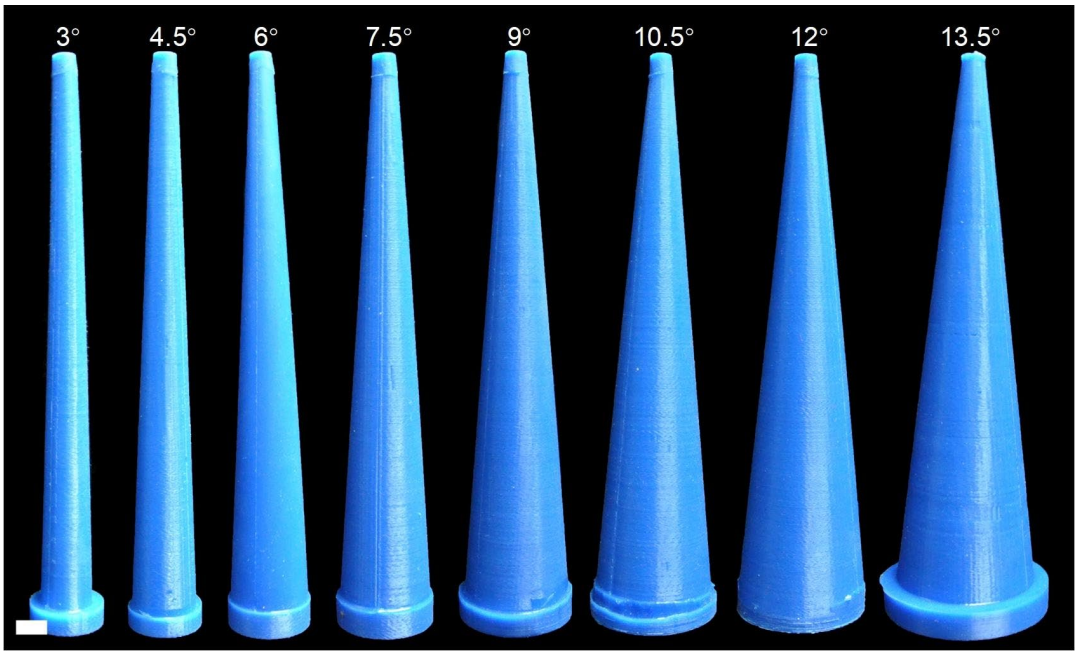

Fig. S7. Tapered soft actuators. Eight tapered soft actuators with taper angle α ranging from 3° - 13.5° were fabricated (scale bar, 10 mm).

To characterize the mechanical response of the silicon rubber used to fabricate our actuators, we tested dog bone-shaped samples (ASTM standard) made out of Mold Star 30 under uniaxial tension, using a single-axis Instron (model 5566, Instron, Inc.) with a 100 N load cell. The material behavior up to a strain of 1.5 (i.e. until failure) is reported in Fig. S8. We find that the material response was effectively captured by an incompressible Gent hyperelastic model (*46*), whose strain energy is given by

$$W = -\frac{\mu J_m}{2}\ln\left(1-\frac{I_1-3}{J_m}\right), \quad [18]$$

where μ is the initial shear modulus of the material, J_m is a constant related to the limiting stretch, and I_1 is the first invariant of the three principal stretch ratios λ_1, λ_2, and λ_3

$$I_1 = \lambda_1^2+\lambda_2^2+\lambda_3^2 \quad [19]$$

The principal nominal stresses s_i can then be obtained as a function of W, λ_i, and the Lagrange multiplier p as

$$s_i = \frac{\partial W}{\partial \lambda_i} - \frac{p}{\lambda_i} \quad [20]$$

Considering a sample subjected to uniaxial stress state and letting the stretch along the axis of loading be $\lambda_1 = \lambda$, incompressibility ($\lambda_1\lambda_2\lambda_3 = 1$) dictates that the stretches in the directions transverse to the loading axis are

$$\lambda_2 = \lambda_3 = \lambda^{-1/2} \quad [21]$$

Next, since there is no stress in the directions transverse to the loading axis

$$s_2 = s_3 = \frac{\partial W}{\partial \lambda_2} - \frac{p}{\lambda_2} = \frac{\mu J_m}{-\lambda^2 - 2\lambda^{-1} + J_m + 3} \cdot \lambda^{-\frac{1}{2}} - \frac{p}{\lambda^{-\frac{1}{2}}} = 0 \quad [22]$$

we find that

$$p = \frac{\mu J_m}{-\lambda^2 - 2\lambda^{-1} + J_m + 3} \cdot \lambda^{-1} \quad [23]$$

By combining equation [20] with [23], we get:

$$s_1 = \frac{\partial W}{\partial \lambda_1} - \frac{p}{\lambda_1} = \frac{\mu J_m}{-\lambda^2 - 2\lambda^{-1} + J_m + 3} (\lambda - \lambda^{-2}) \quad [24]$$

where the stretch λ is related to the applied strain ε as $\lambda = 1 + \varepsilon$. Finally, we fit equation [24] to our measured stress-strain data, and find that the material response is best captured with μ = 195 kPa and J_m = 12 (see Fig. S8).

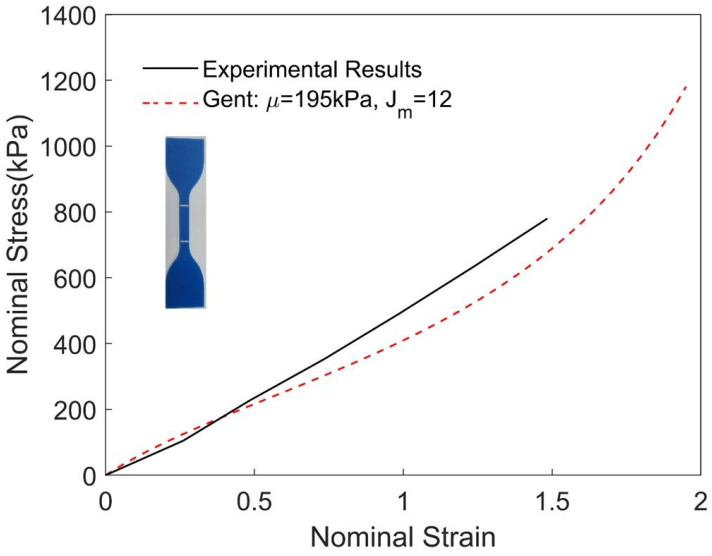

Fig. S8. Material behavior. Stress-strain curve for Mold Star 30 as measured in experiments (continuous line) and predicted using a Gent hyperelastic material model (dashed line).

S4. Experiments on tapered soft actuators without suckers

Bending curvature

Since we were initially unaware of the useful range of motion of the tapered actuator designs (without suckers) and to validate our simulations, we began by investigating the effect of the taper angle on bending curvature for two randomly selected **(cf. Figure F7)** taper angles (α = 6° and α = 10.5°). Each of these actuators were pressurized from P = 0 kPa to P = 200 kPa while

their bases were mechanically immobilized. During inflation, at every 2 kPa increment, we acquired photograph of the actuator deformation, which we processed to extract the minimum, maximum, and average curvatures along the length. Specifically, for each photograph, we identified the line running along the inner gripping side of the actuator (shown in red in Fig. S9) and divided it into 40 equally-sized segments. For the *i*-th segment we then determined the radius R_i of the circle that best fits its bent shape and calculated its average curvature as $\kappa_i = 1/R_i$ (see Fig. S9). From these measurements, we find that, in contrast to the case of cylindrical soft actuators, the bending curvature varies along the length of the tapered actuator – a feature that can be leveraged for grasping differently sized objects. In Fig. S10 we report the evolution of the maximum, minimum, and average curvatures as a function of the applied pressure for the two fabricated actuators, and find that the curvature increases as taper angle decreases.

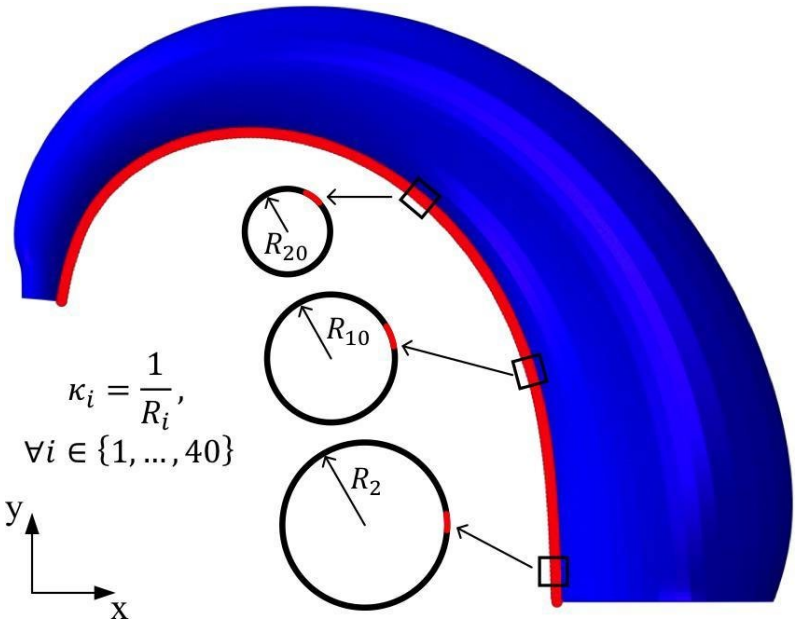

Fig. S9. Curvature (α = 10.5° tapered actuator). Schematic highlighting the procedure used to calculate the bending curvature along the length of the tapered actuator.

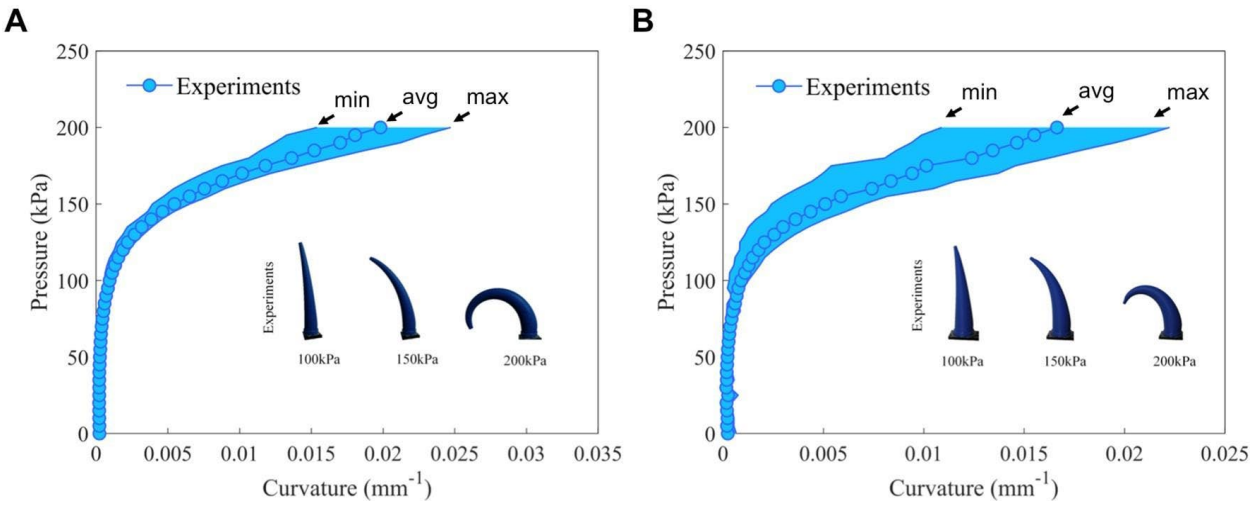

Fig. S10. Experimental results of bending curvature for α = 6° and α = 10.5° tapered actuators. Experimental minimum, average, and maximum curvatures as a function of pressure for tapered actuators characterized by **(A)** α = 6° and **(B)** α = 10.5°. The snapshots of the deformed actuator at different pressures (P = 100 kPa, 150 kPa, and 200 kPa) are shown as insets.

Bending force measurements

Next, we measured the force applied by the actuators upon inflation. To do this, eight actuators with taper angles α = 3°, 4.5°, 6°, 7.5°, 9°, 10.5°, 12°, and 13.5° were tested using the setup shown in Fig. S11A. Specifically, each actuator was fixed at its base and placed at a distance d from a six-axis force transducer (Mini 40 F/T sensor, ATI Technologies Inc., USA). When the actuator would bend upon pressurization, the tip would press against the force transducer to create a tip force, which was acquired by a data acquisition board (PCI 6284, National Instruments Corp., TX, USA) and LabVIEW (National Instruments Corp., 2012) with a sampling frequency of 1000 Hz. For each of the 8 actuators, experiments (N = 5 trials) were conducted for d = 10 mm, 20 mm, 30 mm and 40 mm with pressure input ranging from P = 0 kPa to P = 200 kPa. The experimental results reported in Fig. S11B-E show that for all considered horizontal distances d the bending force increases as both pressure and taper angle increase.

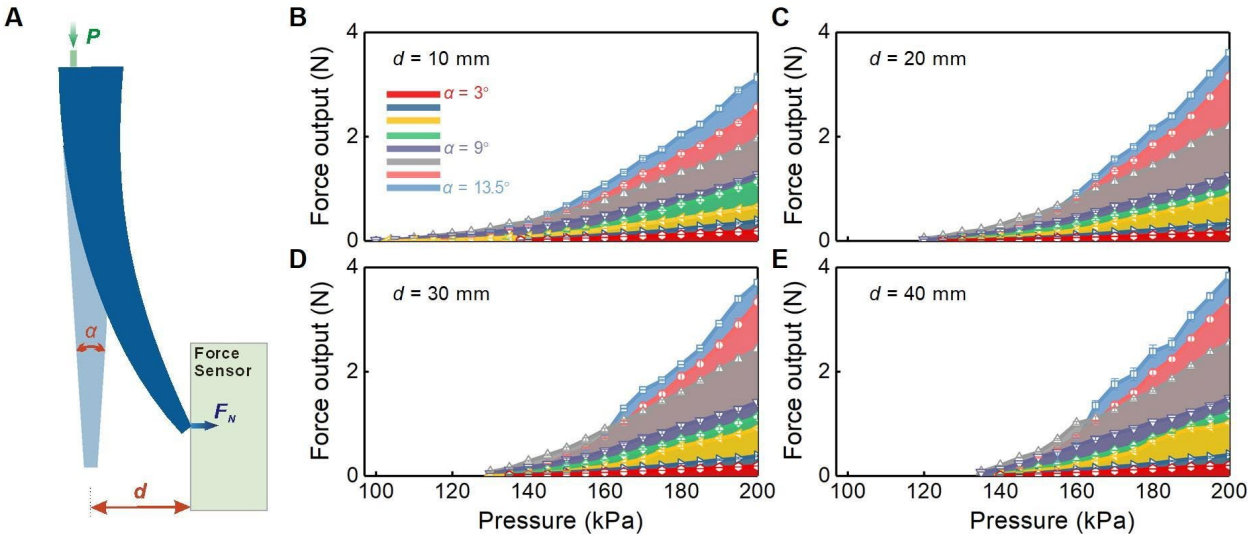

Fig. S11. Experimental results of bending force measurements. (A) Schematic of the setup used to measure the bending force. **(B)-(E)** Bending force (mean ± SE, n = 5) as a function of the applied pressure for soft actuators with different taper angle α (3° to 13.5° with an interval of 1.5°) located at distance **(B)** d = 10 mm, **(C)** d = 20 mm, **(D)** d = 30 mm and **(E)** d = 40 mm from the force sensor.

S5. Numerical simulations

To evaluate the effect of the taper angle on the response of the designed soft actuators (without suckers), static non-linear finite element (FE) simulations were carried out using Abaqus/Standard (SIMULIA, Providence, RI), a commercial finite element software. The models were constructed using 8-node linear brick elements (Abaqus element type C3D8H), and the Gent hyperlastic material model (*46*) (implemented via a UHYPER user subroutine) was used to capture the material response.

Simulating bending in free space

We started by numerically investigating the effect of the taper angle on the bending curvature. In these simulations, the same procedure as the experiments was carried out: the bottom of the actuator was held fixed, a pressure load ranging from P = 0 kPa to P = 200 kPa was applied to the inner chamber, and the minimum, maximum, and average curvatures along the length of the actuators were measured at every 2 kPa (using the same procedure as in experiments). To validate our finite element simulations, we first compared the numerical results to the experimental data shown in Fig. S10. From these measurements, we find that the FE simulation model agrees well with the experimental results obtained from the fabricated actuators (see Fig. S12).

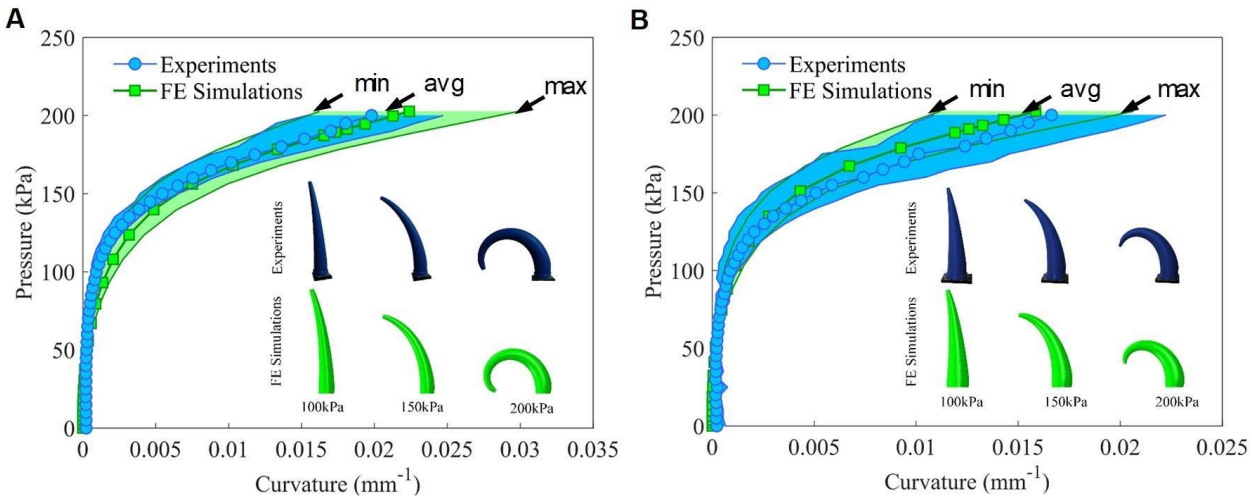

Fig. S12. Comparisons between numerical and experimental results for the bending curvature of the α = 6° and α = 10.5° actuators. Experimental (blue) and numerical (green) minimum, average, and maximum curvatures as a function of pressure for tapered actuators characterized by **(A)** α = 6° and **(B)** α = 10.5°. The snapshots of the deformed actuators at different pressures (P = 100 kPa, 150 kPa, and 200 kPa) are shown as insets.

With the simulations matching the experiments well, numerical modeling could then be carried out to completely and rapidly explore the parameter design space. From exploring this parameter space via FE, we found that the bending curvature of the tapered actuator (including min., avg. and max. κ) depend highly on both the taper angle α and the pneumatic pressure P (Fig. S13A-C). For a given chamber placement (K = 2), we find that the bending curvature increases as pressure P increases, but decreases as the taper angle α increases. For example, the average bending curvature (κ) decreased by over 2-fold (from κ = 0.0282 mm^{-1} to κ = 0.0134 mm^{-1}) by varying the taper angle from α = 3° to α = 13.5° at P = 200 kPa, and changed from κ = 0.0009 mm^{-1} to κ = 0.0134 mm^{-1} by increasing the pneumatic pressure from P = 100 kPa to P = 200 kPa for α = 13.5°.

We also numerically investigated the effect of K (i.e. chamber placement) on the bending curvature by considering an actuator with α = 9°. The results shown in Fig. S13D-F indicate that the bending curvature increases with larger values of K (i.e. for chambers closer to the outer edge of the actuators – see Fig. S13D-F). For example, the average bending curvature (κ) increased roughly 4-fold (from κ = 0.0075 mm^{-1} to κ = 0.0312 mm^{-1}) by varying chamber placement K from 1.75 to 2.5 at P = 200 kPa.

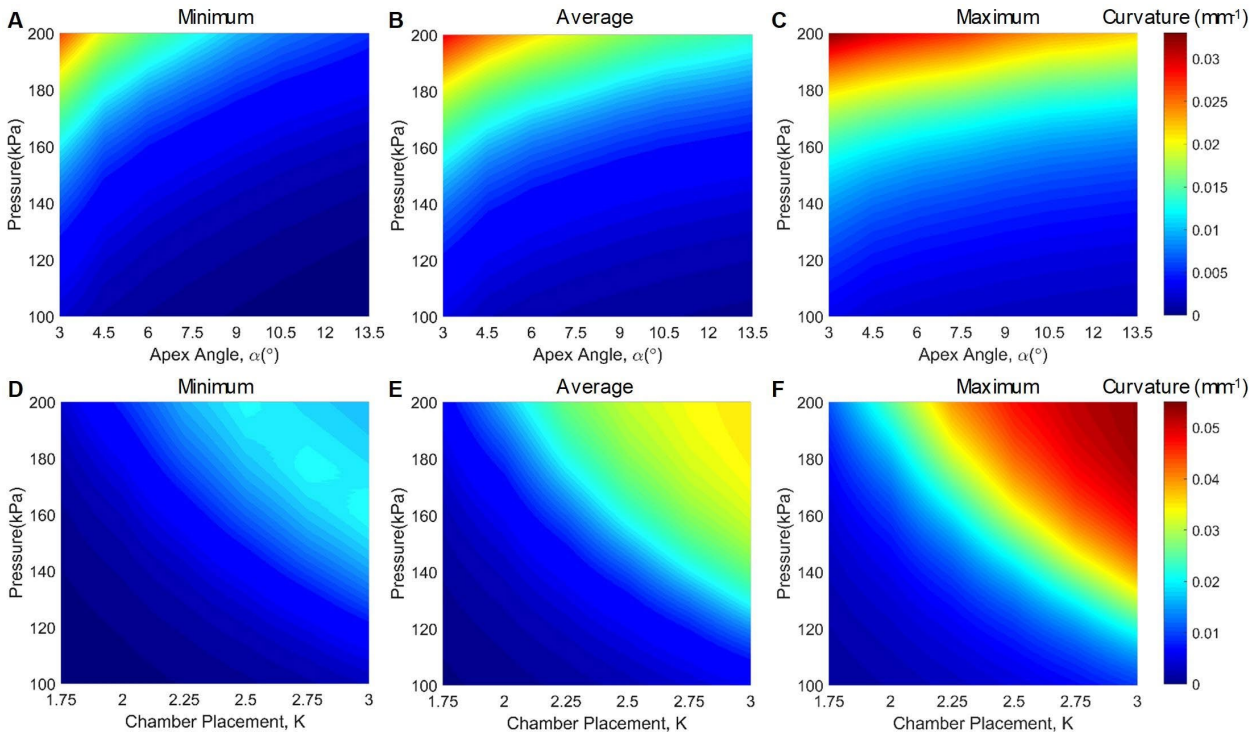

Fig. S13. Simulation results of bending curvature of the tapered soft actuators. Heat map illustrating the minimum **(A)**, average **(B)** and maximum **(C)** bending curvature (κ) as a function of taper angle (α) and input pressure (P), and heat map illustrating the minimum **(D)**, average **(E)** and maximum **(F)** bending curvature (κ) as a function of the chamber placement (K) and input pressure (P).

Simulated bending force

We also investigated numerically the effect of the tapering angle α on the applied bending force. In these simulations, the bottom end of the actuator was held fixed, a pressure load was applied to the surface of the inner chamber (each actuator was pressurized from P = 0 kPa to P = 200 kPa), and the actuators were placed at a horizontal distance (d = 30 mm) away from a rigid body surface. This rigid body surface acted as a hypothetical load cell upon which the actuator could bend and apply force to. Frictional surface to surface contact (coefficient of friction of 0.5) was employed between the rigid body surface and the actuator. As input pressure into the actuator was increased, the actuator would bend towards and apply force to the hypothetical load cell. As shown in Fig. S14, the simulated bending force agrees well with the experimental results obtained from the fabricated actuators. Both the simulated and experimental results indicate that the bending force of the tapered actuator depends highly on both the taper angle α and pneumatic pressure P. Specifically, the bending force increases as pressure P increases and as the taper angle α increases.

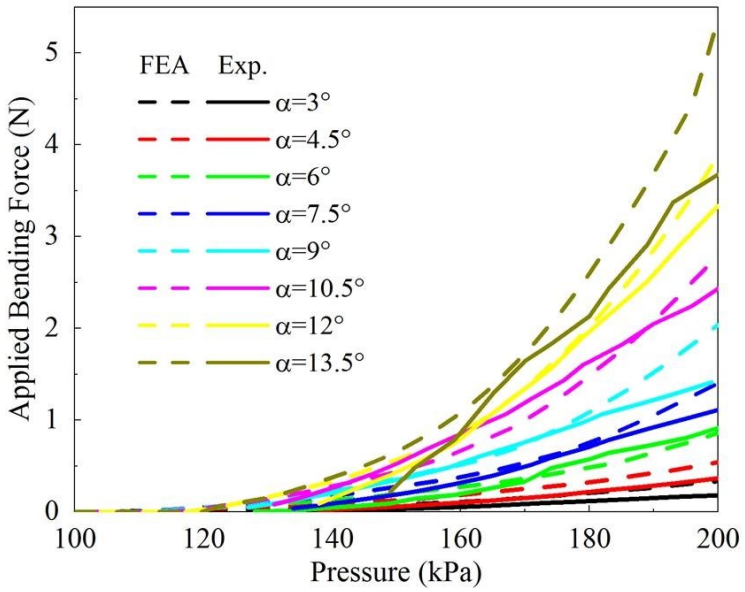

Fig. S14. Comparisons between the numerical and experimental bending forces. Experimental (solid lines) and numerical (dashed lines) results for applied bending force as a function of pressure (up to *P* = 200 kPa) for 8 taper angles. As can be seen from the plot, the numerical bending force results match the experimental results well.

S6. Fabrication of the tapered soft actuator with suckers

A multi-step molding and casting process was used to fabricate the tapered soft actuator with suckers (Fig. S15). As described in section S3, the molds for the casting process were designed in SolidWorks and fabricated using a 3D printer. The difference between the fabrication process of the actuator with suckers and without suckers is the following: when fabricating with suckers, holes were left on the outer tapered actuator mold and threaded with silicone tubes for use in the sucker vacuum generation (Fig. S15A).

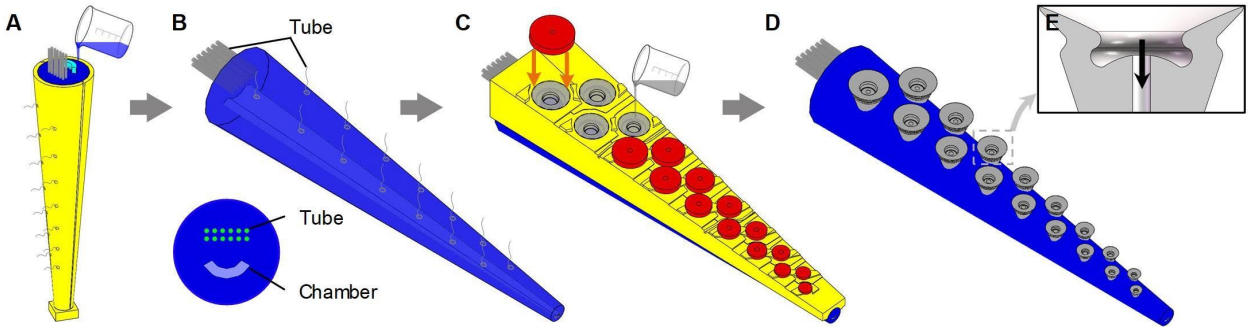

Fig. S15. Fabrication process of the tapered soft actuator with suckers. (A) 3D printed molds are used to cast the robot using elastomer Mold Star 30. **(B)** The cured soft actuator has silicone tubes embedded inside, which were ultimately used to apply a vacuum to the suckers. The cross-sectional view shows the arrangement of the inner arch-shaped chamber and silicone tubes within the actuator. **(C)** A 3D printed mold for the suckers is assembled on the actuator and elastomer was poured into the mold. The 3D printed caps were then laid on the mold to create the shape of the suckers as the elastomer cured. **(D)** The fully cured tapered actuator with suckers was then complete. **(E)** A cross-

sectional view of the suction cup is shown. The aforementioned silicone tubes were embedded within each of the suckers to apply a vacuum (the black arrow indicates the vacuum air flow).

As done before for the fabrication without suckers, after curing, the tapered mold and rod were removed, which created an internal void, which was used as the actuator's inner pneumatic chamber. Additionally, the previously mentioned silicone tubes (for vacuum suction) were left embedded inside the actuator (Fig. S15B). Next to fabricate the suckers onto the actuator with embedded silicone tubes, a 3D-printed mold for casting the suckers was attached to the inside surface of the actuator and tightened to avoid leakage of the fluidic elastomer. Silicone elastomer with Young's modulus of 0.25 MPa (Dragon Skin FX-Pro, Smooth-On Inc., PA) was dyed grey with a coloring agent (Ignite, Smooth-On Inc., PA) and then poured into the mold (Fig. S15C). The elastomer used for the suckers was much softer than that used for the actuator to ensure the flexibility of the suckers. Caps were designed and 3D-printed to fit each sucker's inner infundibulum shape, and a hole was left in the center for a silicone tube to pass through. These caps were placed onto the freshly poured elastomer to create the shape of the suckers and threaded with the silicone tubes previously left in the mold (Fig. S15C). The elastomer was left for 40 minutes at room temperature to cure. After the elastomer cured, the molds were removed. The exposed excess silicone tubes coming out of the suckers were trimmed with scissors, and the actuator was fully sealed with adhesives (Sil-Poxy, Smooth-On Inc., PA) (Fig. S15D). The fabrication process of the cylindrical gripper was the same for the tapered gripper. The fully fabricated tapered soft actuators with suckers are shown in Fig. S16.

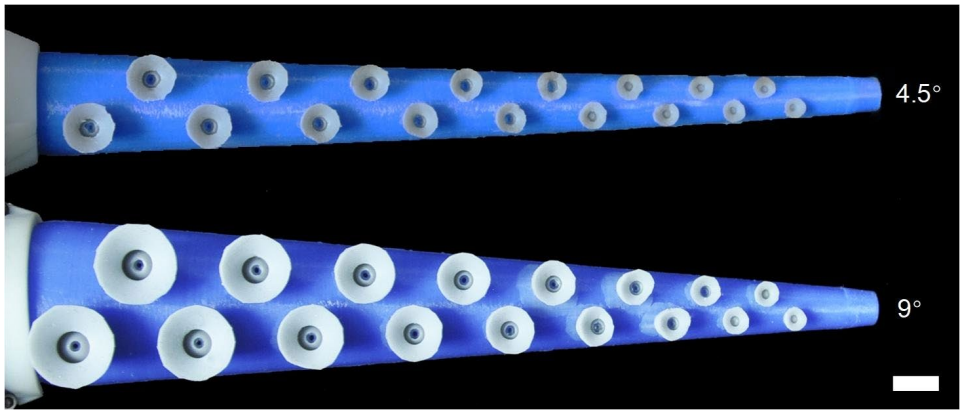

Fig. S16. Two tapered grippers with taper angle α = 4.5° and α = 9° (scale bar, 10 mm).

The 3D-printed clamps were then mounted on the actuator, and two air connectors were left for the actuation of bending and suction, respectively. Moreover, to improve the human-machine interface, we developed an integrated hand-held controller to allow simple manipulation of the tapered soft actuator with suckers. Two on-off valves and a vacuum generator were placed in a 3D-printed bulb-shaped shell (60 mm in diameter), and wo buttons were installed on the handle to independently control the bending and suction (Fig. 5B).

The fabricated α = 9° tapered soft actuator with suckers was actuated at a pressure of P = 200 kPa and compared with α = 9° tapered actuator without suckers actuated at the same pressure. The results show no distinct difference between the bending of the α = 9° tapered

actuator with and without suckers (Fig. S17), demonstrating that the fabricated suckers do not alter the actuator's bending during pressurization.

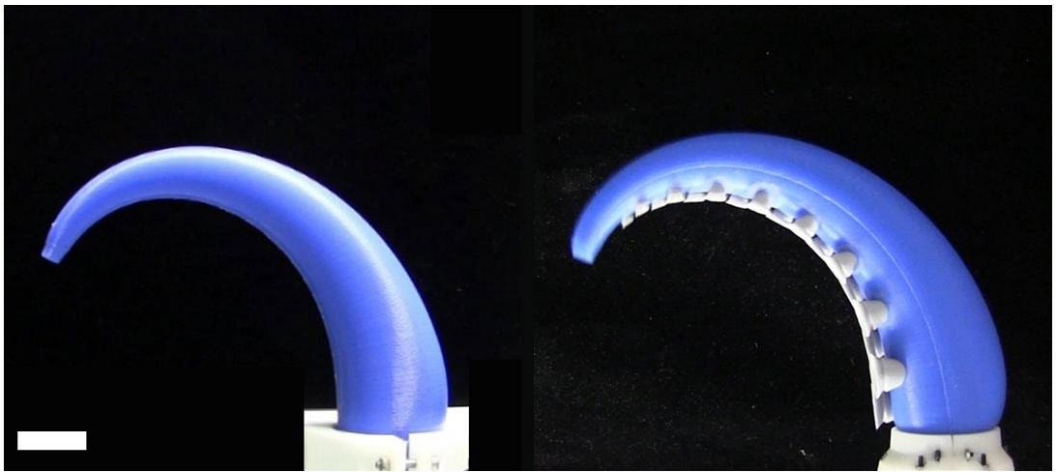

Fig. S17. Bending comparisons between actuators with and without suckers at P = 200 kPa. This result demonstrates that the suckers do not alter the actuator's bending during pressurization (scale bar, 2 cm).

S7. Sucker attachment force measurements

In this section, we detail the sucker attachment force measurements for the α = 4.5° and α = 9° tapered actuators with suckers. We investigated the engagement of the suckers on three planar surfaces of different roughnesses (R_a < 1 μm, 20 μm, 200 μm) as well as one curved surface of roughness R_a < 1 μm.

Experimental substrates

Four surfaces (three planar surfaces of increasing roughness: R_a < 1 μm, 20 μm, 200 μm, and then also one smooth surface, R_a < 1 μm, with a curvature of 1/260 mm^{-1}) were used in this study. To control for the effects of material stiffness, wettability, surface chemistry, and temperature, and to focus on the effect of surface roughness alone on adhesion with the suckers, the surfaces were all fabricated with the same epoxy resin material (EpoxAcast 650, Smooth-On Inc., PA, USA).

To create the substrate surface with R_a ~20 μm roughness, a mold was created from sandpaper with the desired roughness (FEPA Grit designation P600, corresponding to an average particle diameter of ~20 μm) from Dragon Skin 20. Next, casting epoxy was poured into the Dragon Skin 20 mold, allowed to cure for 24 hours, and removed. The same procedure was then used to create another substrate surface with a roughness of ca. R_a ~200 μm (FEPA Grit designation P80 sandpaper, corresponding to an average particle diameter of ~200 μm). Finally, the smooth flat substrate surface (R_a < 1 μm) was created with a mold made from glass. The three flat substrates were then fastened to a 3D-printed plastic base plate fixed onto a force transducer to measure suction force (Fig. 4C insert panel).

For the smooth surface with a curvature of 1/260 mm^{-1}, casting epoxy was poured into the glass mold as was done before for the flat surface and allowed to cure for 12 hours, after which

the substrate surface was semi-solidified. The substrate was then removed from the glass mold and laid on a 3D-printed plastic base plate with curvature of 1/260 mm^{-1}. Because of its semi-solidified state, the substrate surface cured over the next 12 hours to the same curvature as that of the plastic base plate (1/260 mm^{-1}). The curved substrate was also fastened to the 3D-printed base plate and fixed to the force transducer.

Experimental setup for measuring sucker attachment force

To measure the actuator's sucker attachment force, we designed and built the system shown in the Fig. 4C inset schematic. A six-axis ATI force transducer (Mini 40 F/T sensor, ATI Technologies Inc., USA) was mounted to an imobile base plate with its *z*-axis parallel to the ground. A 3D-printed plastic base was fixed on the force transducer with one of the four substrate surfaces (whichever was currently being tested) fastened to it. The actuator was then mounted with its base fixed to a robotic arm (MOTOMAN MH3F, YASKAWA Inc., Japan). For the suction force measurements on the three flat surfaces, the actuator's suckers were positioned parallel to the substrate, the tapered actuator was not inflated, and only the sucker vacuum (-80 kPa) was applied to attach to actuator to the substrates (the initial position of the robotic arm is shown in Fig. 4A). For the curved surface measurements, the actuator's most proximal sucker was initially positioned adjacent to the edge of the grasped object and engaged with the surface (while the rest suckers were not in contact) (Fig. 4E). The tapered actuator was subsequently pressurized (P = 0 kPa to P = 240 kPa with an interval of 10 kPa) to adapt to the substrate curvature, and the sucker vacuum (-80 kPa) was then applied (Fig. 4D, inserted schematic). The robotic arm was programmed to move vertically upwards at a constant speed of 0.1 mm/s until the suckers completely lost contact with the substrate surface. For each experiment, N = 3 trials were conducted for statistical purposes. The force data were acquired by a data acquisition board (PCI 6284, National Instruments Corp., TX, USA) and LabVIEW (National Instruments Corp., 2012) with a sampling frequency of 1000 Hz.

Results of the sucker attachment force measurements

The peeling-off process of the α = 4.5° actuator from its base on the smooth flat surface are provided in Figs. S18A, B. Just as was the case with the α = 9° actuator as discussed in the main text, the α = 4.5° gripper was also able to successfully attach to surfaces exhibiting a wide range of surface roughnesses and the results are shown in Fig. S18C. The α = 4.5° gripper required a pull-off force of 1.31 ± 0.08 N on a smooth surface, 1.86 ± 0.09 N on a medium-roughness surface (R_a = 20 μm), and 0.81 ± 0.06 N on a rough surface (R_a = 200 μm) (Fig. S18C). Finally, we also investigated the effects of bending on the adhesive performance of the α = 4.5° gripper on a curved surface (1/260 mm^{-1}) under different pneumatic pressures, the results from which, can be found in Fig. S18D. Similar to the α = 9° gripper (as shown and discussed in the main text), the attachment of the α = 4.5° gripper to the surface is highly dependent on the pressure input since this determines how many suckers engage to the surface. After determining the optimal pressure (P = 130 kPa) for this combination of actuator and surface curvature (Fig. S18D), this pressure was then used to obtain the results shown in Figs. S18E, F. Looking at these pull-off force results, we see that the actuator can achieve a pull-off force similar on both flat (1.31 ± 0.08 N) and curved surfaces (1.85 ± 0.05 N), as all suckers made full contact with both surfaces (Figs. S18A, B and S18E, F).

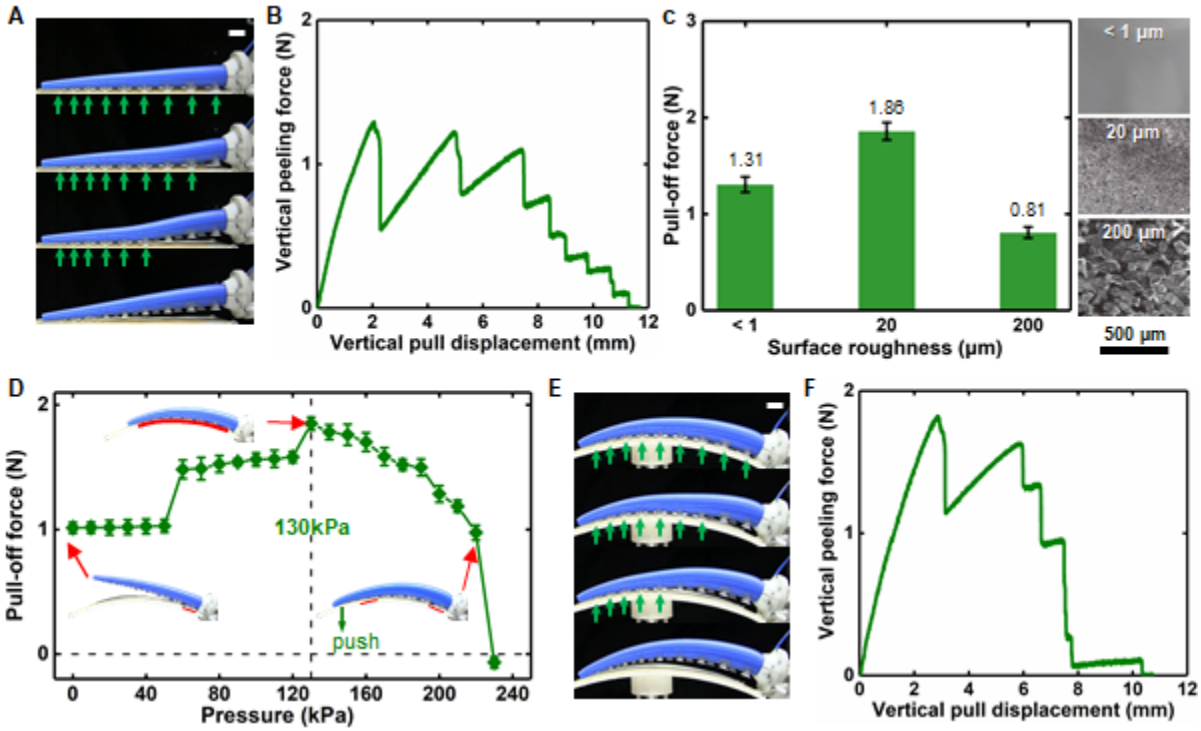

Fig. S18. Attachment force of the α = 4.5° gripper against different surfaces. Side-view photographs **(A)** showing the sequential pull-off of an α = 4.5° tapered gripper actuated from a smooth planar surface and its corresponding load-displacement curve **(B)**. **(C)** The attachment forces of the α = 4.5° tapered gripper on planar surfaces of various roughness (R_a: < 1 μm, 20 μm, 200 μm). **(D)** Scanning a wide range of input pressures with the α = 4.5° tapered gripper permits the identification of the optimal input pressure (and therefore curvature) for maximizing pull-off force from non-planar substrates. The vertical dashed line indicates the "critical" pneumatic pressure values for maximizing the pull-off forces of the α = 4.5° tapered gripper for the curvature of this specific surface (260 mm^{-1}). Side-view photographs showing the sequential pull-off of the α = 4.5° tapered gripper actuated from a smooth curved surface **(E)** and its corresponding load-displacement curve **(F)**.

We also compared the pull-off force of the tapered actuator and the cylindrical actuator with identical suckers in terms of both size and distribution (Fig S19A). As shown in Fig. S19B and S19C, the suckers of the cylindrical gripper peel off nearly simultaneously from the planar surface, resulting in a sharp and sudden failure compared to the tapered design. This failure mode was also observed for curved surfaces, despite the fact that an optimal input actuation pressure was selected (such that the actuator's curvature most closely approximated that of the grasped object) to maximize the peeling force (Fig. S19D,E). Even so, the cylindrical gripper has a sharper and quicker drop in force as all the suckers peel off more simultaneously (Fig. S19F). This supports the overall conclusion that the tapered actuator with suckers has better gripping capabilities than the cylindrical-shaped actuator, even when they have an identical sucker size and pattern.

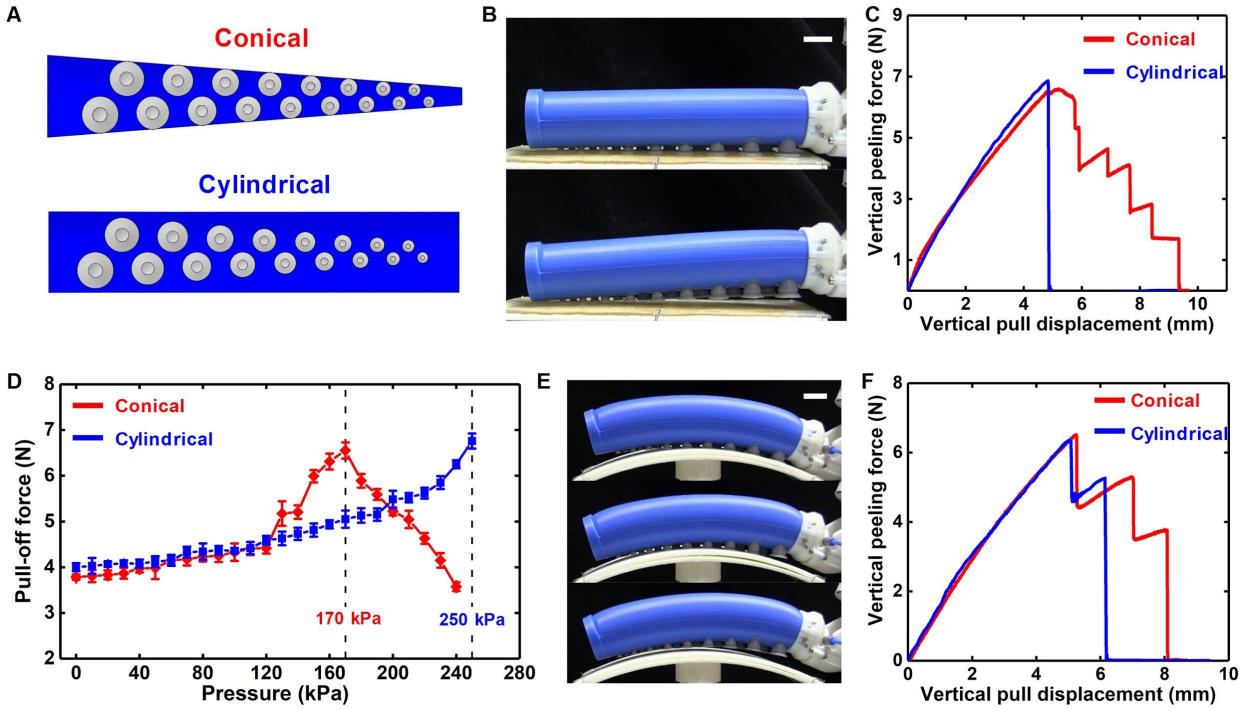

Fig. S19. Sucker attachment force measurements of the cylindrical actuator with suckers that of the same size and spatial distribution as those from the tapered actuator. **(A)** The CAD model of the 9° tapered actuator with suckers and a corresponding cylindrical actuator with the same sucker size distribution and placement. (**B**) Side-view photographs showing the simultaneous peeling of the cylindrical actuator with suckers from a smooth planar surface (scale bar, 20 mm). **(C)** Load-displacement curves recorded during the peeling test for both the tapered and cylindrical actuators with suckers. **(D)** Scanning a wide range of input pressures permits the identification of the optimal input pressures for maximizing pull-off forces of both actuators with suckers from non-planar substrates. The vertical dashed line indicates the "optimal" pneumatic pressure values for maximizing the pull-off forces for the curvature of this specific surface (260 mm^{-1}). **(E)** Side-view photographs showing the sequential peeling of the cylindrical actuator with suckers from a smooth curved surface (scale bar, 20 mm). **(F)** Load-displacement curves recorded during the peeling test for both the tapered and cylindrical actuators with suckers.

S8. Tapered gripper demonstrations

Fig. S20 shows the inflation and vacuum pressure time series of the tapered gripper during a semi-autonomous "attach, wrap, transport, and deliver" process as discussed in the main text. As Fig. 6A shows, the α = 4.5° gripper was mounted on the robotic arm. Starting with the non-pressurized α = 4.5° tapered gripper (t = 0 s), the robotic arm was first programed to reach the plastic sheet and a -60 kPa vacuum was applied to the suction cups (t = 2 s). Once the suckers were attached to the plastic sheet, the vacuum pressure rapidly raised to -80 kPa (t = 4 s), and the system detected the pressure change from the suckers. Next, a 2-second time delay is set for the robotic arm to lift the attached plastic sheet. The gripper was then pressurized (P = 250 kPa) to "wrap" the sheet into a roll (t = 6.5 s). After that, the robotic arm transported the sheet quickly (t = 8 s) in a programmed trajectory and then delivered it to a human hand at t = 12 s (the vacuum and inflation pressure returned to P = 0 kPa at this time). In this process, the suckers not only worked to assist grasping, but also acted as feedback elements for the control system. With the

pressure sensory feedback principle demonstrated here, our gripper could likely be used for a wide range of industrial applications, especially those involving direct human interaction.

We next investigated the bending kinematics and velocity of the tapered gripper. Based on the tradeoff (between bending curvature and applied bending force) as a function of taper angle we presented earlier, the $\alpha = 4.5°$ and $\alpha = 9°$ grippers show obvious different characteristics. To compare the bending kinematics and velocity of actuators with different taper angles, we actuated each gripper ($\alpha = 4.5°$ and $\alpha = 9°$) with a miniature compressor (LRMA-QS-4, FESTO Inc), which delivered compressed air at a maximum flow rate of 40 L/min (Movies S4 and S5). This compressor fully bent the $\alpha = 9°$ gripper in 1.2 ± 0.11 seconds ($N = 5$) and the $\alpha = 4.5°$ gripper in 0.3 ± 0.06 seconds ($N = 5$). Fig. S21A shows snapshots taken from movies (Movies S6 and S7) of the two actuators bending. The $\alpha = 4.5°$ gripper showed an interesting and potentially useful spiral bending behavior with the tip of the actuator curling past its own base.

It should be noted that the spiral shape is due to the actuator's taper angle, whereas a traditional cylindrically-shaped actuator self-intervenes by coming into contact with its own base at high pressures (Fig. S22). However, despite the bending kinematics and velocity, the $\alpha = 9°$ actuator has an advantage in terms of applied grasping force. As shown in Fig. S21B, we actuated the $\alpha = 9°$ gripper at a pressure of $P = 250$ kPa, and the $\alpha = 9°$ gripper was able to lift a bucket of water weighing up to 27 N — over 24 times the weight of the prototype.

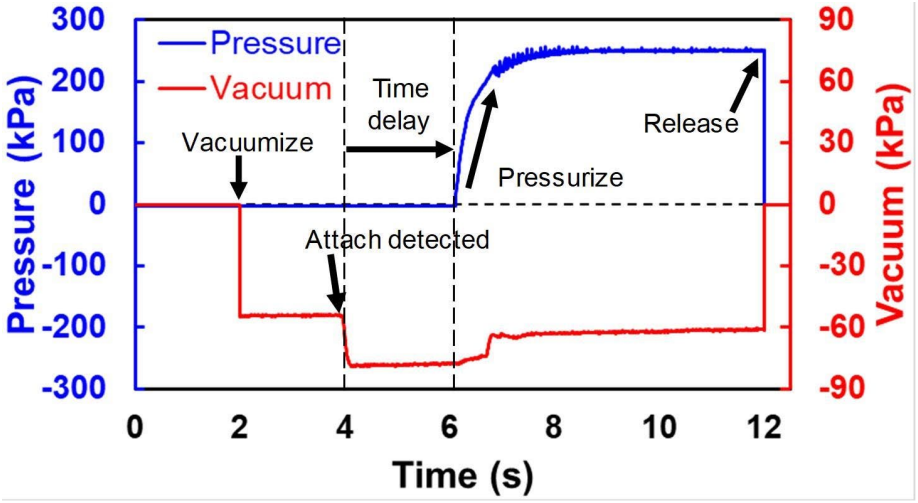

Fig. S20. The inflation and vacuum pressures as a function of time during the "attach, wrap, transport, and deliver" process. Starting with the non-pressurized $\alpha = 4.5°$ tapered gripper (t = 0 s), a vacuum was first applied to the suction cups (t = 2 s), the system detected the pressure change from the suckers at t = 4 s, and after 2-seconds' time delay (time for the robotic arm lifting up the attached plastic sheet) the actuator was then pressurized ($P = 250$ kPa) to "wrap" the sheet into a roll (t = 6.5 s). The robotic arm then transported the sheet quickly (t = 8 s) and delivered it to a human hand at t = 12 s (the vacuum and inflation pressure returned to $P = 0$ kPa).

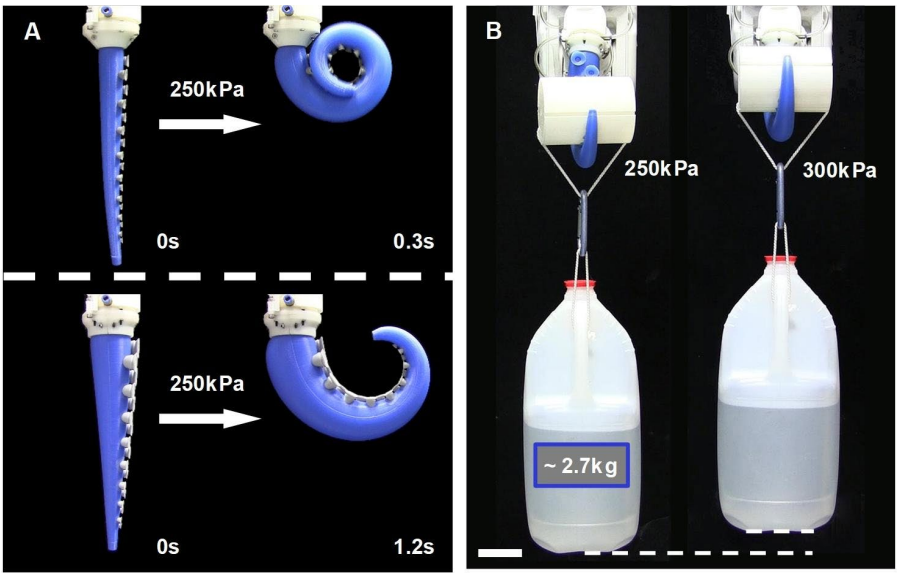

Fig. S21. Motion of $\alpha = 4.5°$ and $\alpha = 9°$ grippers and load capability of $\alpha = 9°$ gripper. (A) Individual frames from a high-speed video of the initial and final positions of the actuators when pressurized from $P = 0$ kPa to $P = 250$ kPa. The $\alpha = 4.5°$ gripper bent into a spiral shape (upper) while the $\alpha = 9°$ gripper bended into an arc with non-uniform curvature (lower). The $\alpha = 4.5°$ gripper displayed a faster response (t = 0.3 s) than the $\alpha = 9°$ gripper (t = 1.2 s). **(B)** The $\alpha = 9°$ gripper can lift up a weight of 2.7 kg at input pressures of $P = 250$ kPa (left) and $P = 300$ kPa (right) (scale bar, 5 cm).

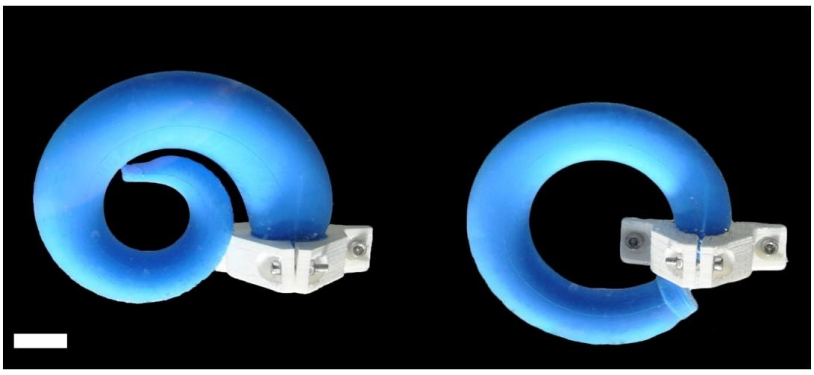

Fig. S22. Bending comparisons: tapered and cylindrical soft actuator (without suckers). (scale bar, 2 cm).